Effect of redox conditions of glass melting on the structure and the properties of titanium-containing gahnite glass-ceramics

Kirill Eremeev[1], Olga Dymshits[2,3]*, Irina Alekseeva[3], Alexander Khubetsov[3], Svetlana Zapalova[3], Marina Tsenter[3], Liza Basyrova[1], Josep Maria Serres[4], Xavier Mateos[4,#], Pavel Loiko[1], Vadim Popkov[2], Aleksandr Zhilin[5]

[1] Centre de Recherche sur les Ions, les Matériaux et la Photonique (CIMAP), UMR 6252 CEA-CNRS-ENSICAEN, Université de Caen Normandie, 6 Boulevard Maréchal Juin, 14050 Caen, France
[2] Ioffe Institute, 26 Politekhnicheskaya, St Petersburg, 194021, Russian Federation
[3] Vavilov State Optical Institute, 36 Babushkina St., St Petersburg, 192171,Russian Federation
[4] Universitat Rovira i Virgili, URV, Física i Cristal·lografia de Materials i Nanomaterials (FiCMA-FiCNA), Marcel·lí Domingo 1, 43007 Tarragona, Spain
[5] D.V. Efremov Institute of Electrophysical Apparatus, 3 Doroga na Metallostroi, pos. Metallostroi, St Petersburg, 196641, Russian Federation

* Corresponding author. *E-mail address:* vodym1959@gmail.com (O. Dymshits).

Abstract

In order to develop glass-ceramics containing ions of variable valence in lower oxidation states, it is important to know how changing the redox conditions of glass melting affects structure and properties of glass-ceramics. The zinc aluminosilicate glass nucleated by TiO_2 was melted with and without addition of As_2O_3 and heat-treated from 720 to 1350 °C to obtain gahnite-based glass-ceramics. DSC, XRD analysis, Raman spectroscopy and TEM studies revealed that variation of glass melting redox conditions affects kinetics of liquid phase separation and rutile crystallization, composition and structure of gahnite and rutile, crystallization of the residual glass, and does not affect kinetics of gahnite crystallization, gahnite and rutile fractions and structure of glass-ceramics. In glass-ceramics prepared from glasses melted without As_2O_3, absorption in the visible and near-IR spectral ranges is due to octahedrally coordinated Ti^{3+} ions in gahnite nanocrystals. The study is important for development of rare-earth-free phosphors.

Keywords: redox conditions; glass-ceramics; gahnite; structure; spectroscopy.

1. Introduction

Cubic crystals with spinel structure, both natural and synthetic, demonstrate unique properties of high isomorphic capacity, hardness, chemical and thermal resistance. The structural formula of oxide spinel is $^{IV}[A_{1-\delta}B_{\delta}]^{VI}[B_{2-\delta}A_{\delta}]O_4$, in which A and B are divalent, trivalent, or quadrivalent cations. $^{IV}[]$ and $^{VI}[]$ denote tetrahedral and octahedral positions respectively, and δ is an inversion parameter. Spinels have a face-centered cubic unit cell, which consists of 8 formula units and contains 32 oxygen anions arranged in a cubic close-packed lattice with 64 tetrahedral

and 32 octahedral positions per the unit cell. Spinels belong to the space group Fd-3m. When 8 A^{2+} ions occupy 1/8 of all tetrahedral sites, and 16 B^{3+} ions occupy half of all octahedral sites, the spinel is called the "normal" one ($\delta = 0$). In the "inverse" spinel ($\delta = 1$) half of the B^{3+} ions are in tetrahedral sites; the other half of the B^{3+} and all A^{2+} ions are distributed between octahedral sites. The principle member of spinel family is normal magnesium aluminate spinel with the composition $MgAl_2O_4$.

Zinc spinel, gahnite, with the composition of $ZnAl_2O_4$ also belongs to the family of aluminate spinels. Zinc spinel has attracted much attention because of its promising optical, electronic, catalytic, and dielectric properties and irradiation tolerance [1-3]. Gahnite is a suitable matrix for doping with transition metal ions, such as Cr^{3+}, Fe^{2+}, Fe^{3+}, Ni^{2+}, Co^{2+}, Ti^{4+}, Mn^{2+} [4-13]. Gahnite can be produced by different methods in the form of single crystals [14-17], optical ceramics [18-24], nanoparticles [25] or as a crystalline phase in glass-ceramics (GCs) [24,26-37]. Zinc spinels, both natural [7] and synthetic [14,38-42], demonstrate some degree of inversion, which depends on the synthesis method [41], shows temperature dependence [39-42] and influences the properties of gahnite [40,41].

Each method of gahnite synthesis has its own advantages and disadvantages. Production of $ZnAl_2O_4$ single crystals from the melt is time consuming and difficult because of high vapor pressure of zinc oxide [14,16,17]. Several research groups are involved in development of transparent gahnite-based ceramics, both undoped [17-22] and doped [23,24]. Although a significant progress has been made in this field, transparent gahnite-based ceramics doped with transition metal ions are still porous and have low laser damage threshold, which prevents their use as saturable absorbers [23,24]. Gahnite nanocomposites suffer from agglomeration and aggregation of nanoparticles that significantly deteriorate their properties.

Transparent GCs based on nanosized gahnite crystals [24,26-37], in comparison with nanoparticles, single crystals and transparent ceramics, have advantages of the optical glass manufacturing technology, which provides the possibility of scalable production of highly homogeneous materials with nanocrystals of a variety of compositions, physical and chemical properties, structures and sizes. GCs are produced by controlled crystallization of glasses of specially developed compositions, as a rule, containing a nucleating agent. The phase composition of the GC, the growth rate and the size of crystals are determined by the composition and heat-treatment schedule of the initial glass. The glass formation region, the field of gahnite crystallization and phase transformations in the ZnO-Al_2O_3-SiO_2 system have been studied in Refs [28,43-47].

Addition of a nucleating agent is necessary for the development of highly transparent gahnite-based GCs with reproducible phase composition and properties and with minimum

absorption. Among other nucleating agents, TiO_2 is the most frequently used for bulk crystallization of gahnite [29-34,36]. It is well known that titanium ions exist in two oxidation states, Ti^{3+} and Ti^{4+}. The ratio of concentrations of Ti^{3+} and Ti^{4+} ions in the glass melt is influenced by the redox conditions of glass melting. It is known that glass melting at high temperatures in the absence of oxidizing agents promotes appearance of Ti^{3+} ions [48]. It results in grey coloration of transparent gahnite-based GCs [29,34]. Transparent GCs without grey coloration were obtained due to addition of arsenic oxide to keep a high ratio of Ti^{4+} to Ti^{3+} in the glass and glass-ceramic, thereby minimizing any color [30]. As a rule, initial glasses for the development of transparent gahnite-based GCs for optical applications are melted with the addition of As_2O_3 to achieve weakly oxidizing conditions. Recently, attempts were made to substitute the arsenic oxide with less toxic refining agents. A.R. Molla *et al.* [34] demonstrated the effect of CeO_2 as an oxidizing agent eliminating the dark brown coloration (caused by the Ti^{3+} ions) of transparent glasses of the ZnO-Al_2O_3-SiO_2-TiO_2 system and GCs prepared from these glasses, but A.R. Molla *et al.* [34] did not compare properties of GCs obtained from glasses melted in oxidizing and reducing (redox) conditions. We are not aware of any study devoted to the influence of redox conditions and, consequently, of titanium oxidation state on the phase composition, structure and optical properties of GCs containing nanosized gahnite crystals.

We have found the works [49,50], in which the phase decomposition and crystallization of titanium-containing glasses obtained under different redox conditions were compared, but these glasses were of the magnesium aluminosilicate and fresnoite systems. W. Vogel [49] presented the crystallization sequence of two glasses from two different crystallization fields. The first glass from the cordierite field contained 5 mol% TiO_2. The second glass from the mullite field contained 8.3 mol% TiO_2. Both glasses were melted under normal and reducing conditions. Though the final crystalline phases in GCs of the same composition were either cordierite, or mullite, regardless the redox conditions of the glass melting, the intermediate phases and crystallization temperatures were partly different, the difference being more significant for the glass of the first composition. Holand *et al*. [50] demonstrated that the difference in compositions of intermediate crystalline phases resulted in different mechanical properties of obtained GCs.

The role of Ti^{3+} ions in the nucleation and growth of fresnoite crystals from the melts of the BaO – TiO_2 - SiO_2 system was studied in [48,51,52].

The aim of the present study is to investigate the effect of redox conditions on the phase composition, structure and optical properties of gahnite-based GCs nucleated by titania. It is important for understanding and interpreting the processes that occur when ions of elements with variable valence are introduced into titanium-containing zinc aluminosilicate glasses subjected to secondary heat-treatments. It will help one to develop GCs doped with such ions in desired,

especially in the lower oxidation states. For instance, GCs containing nanosized Fe^{2+}:$ZnAl_2O_4$ crystals can be promising for saturable absorbers of lasers operating in the spectral range of 2 μm [50]. To make GCs containing Fe^{2+} ions, reducing conditions of initial glass melting are required. It is important to know whether the reducing conditions of glass melting modify the structure and phase composition of GCs and deteriorate their transparency, or not.

Searching for rare-earth-free phosphors is an urgent task because of the large increase in prices of rare-earth oxides [53]. Ti^{3+} ions in crystals and glasses are known for their broadband emission in the visible and near-IR spectral range [54,55], which could be used for tunable laser applications. There is no literature data on studies of Ti^{3+}-doped $ZnAl_2O_4$ by now. Development of transparent GCs containing Ti^{3+} ions in gahnite nanocrystals could help to elaborate such materials. This study is important for the development of rare-earth-free Ti^{3+}-doped phosphors with the broadband emission.

2. Experimental

2.1. Synthesis of glass-ceramics

The model glass with the composition 25 ZnO, 25 Al_2O_3, 50 SiO_2 (mol%) nucleated by 9 mol% TiO_2 introduced above total 100% [32,56] was melted with and without addition of 0.5 wt% As_2O_3. The reagent grade oxides ZnO, Al_2O_3, SiO_2, TiO_2, and As_2O_3 were used as raw materials. We did not add any other component to the glass. The glasses were named ZAS_{ox} and ZAS, where ZAS_{ox} stands for the glass melted in oxidizing conditions, with the addition As_2O_3, and ZAS stands for that melted under normal conditions, without addition of As_2O_3. The addition of As_2O_3 can result in following reactions in the process of glass melting [49,57]

$$As_2O_3 + O_2 \rightarrow As_2O_5 \text{ (1000 °C);}$$

$$As_2O_5 \rightarrow As_2O_3 + O_2 \text{ (1200 – 1700 °C)}$$

The residual oxygen formed during glass melting can oxidize Ti^{3+} to Ti^{4+} [34].

In spite of the fact that the second reaction is reversible upon cooling of the homogeneous glass melts, we believe several reasons can be responsible for preventing the expected reduction of Ti^{4+} ions in the presence of As_2O_3 upon cooling the ZAS glass melts. On the one hand, the glass is melted at temperature of 1580 °C and quickly quenched from this temperature, which, given the high viscosity of the melt, allows its high-temperature structure to be frozen. On the other hand, the resulting glass reveals a nanoinhomogeneous structure and contains liquid phase-separated regions enriched in titanium ions [32], which indicates that the redox equilibria in this case differ from those observed during cooling of homogeneous melts.

Batches to obtain 400 g of glass were melted in crucibles made of quartz ceramics in a laboratory electric furnace at 1580 °C for 4 h with stirring by stirrers made of the same material.

The glass melts kept at the temperature of 1580 °C were poured onto a cold metal plate and annealed at 680 °C. Then they were subjected to two-stage heat-treatments with the first hold at 720 °C [54] and the second one at temperatures from 750 to 1350 °C with a holding time of 6 hours (h) at each stage.

Figure 1 demonstrates the images of the initial glasses and GCs. The ZAS glass is slightly grey colored while the ZAS_{ox} glass has a very pale straw yellow coloration. Glasses heat-treated at 720 °C for 6 h and by two-stage heat-treatments with the second hold at temperatures from 750 to 1050 °C are transparent. Their grey and pale straw yellow coloration increased with increasing the heat-treatment temperature. The GCs prepared with the second hold at 1100 °C are translucent, near opaque, while the CGs prepared by the second hold in the range from 1200 to 1350 °C are opaque, see Fig. 1. The ZAS sample has an easily removable surface layer after heat-treatment at 1300 °C. This sample cracked after the heat-treatment at 1350 °C (not shown here). The ZAS_{ox} sample cracked after heat-treatments at 1300 and 1350 °C. This destruction is due to the transformation of β-cristobalite crystals to α-cristobalite upon cooling these samples, see below.

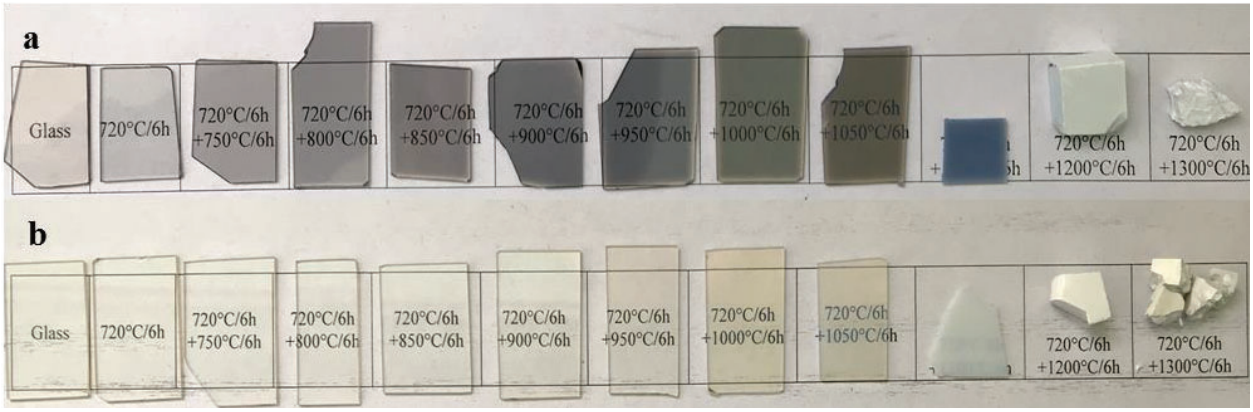

Fig. 1. Photographs of the polished initial glasses, glasses produced by the heat-treatment at 720 °C and glass-ceramics produced by the two-stage heat-treatments with the first hold at 720 °C and the second hold from 750 to 1300 °C. Holding time at each stage is 6 h. (a) ZAS samples; (b) ZAS_{ox} samples. The thickness of the polished samples is 1 mm.

2.2. Characterization of glasses and glass-ceramics

The sequence of phase transformations in initial glasses was determined by the differential scanning calorimetry (DSC) method. For the DSC study, bulk samples of the quenched initial glasses and annealed glasses heat-treated at the nucleation stage of 720 °C for 6 h about 20 mg in weight were used. A simultaneous thermal analyzer NETZSCH STA 449 F3 Jupiter with a dynamic flow atmosphere of Ar was employed. The temperature range was from room temperature to 1200 °C, and the heating rate was 10 °C·min^{-1}.

X-ray diffraction (XRD) patterns of powdered samples were recorded by a Shimadzu XRD-6000 diffractometer with Cu Kα radiation (λ = 1.5406 Å) and a Ni filter. The parameters of the unit cell *a* of gahnite nanocrystals were determined using the diffraction peak with the Miller's indices (440) at $2\theta \approx 65.5°$ according to the equation:

$$a = d_{hkl} \cdot \sqrt{h_2 + k_2 + l_2}, \quad (1)$$

where d_{hkl} is an interplanar distance in Å, and *h, k* and *l* are the Miller's indices.

The parameters of the unit cell of rutile nanocrystals were determined using diffraction peaks with the Miller's indices (110) and (211) at $2\theta \approx 27.27°$ and $2\theta \approx 54.2°$, respectively, according to the equation (1) for parameter *a*, and according to the equation (2) for parameter *c*:

$$\frac{1}{d_{hkl}^2} = \frac{h^2 + k^2}{a^2} + \frac{l^2}{c^2} \quad (2)$$

The error in the estimation of the unit cell parameters was ± 0.003 Å.

The mean crystal sizes were estimated from broadening of the X-ray diffraction peak at 2θ ≈ 65.5° for gahnite, and at 2θ ≈ 27.27° for rutile according to the Scherrer equation [58] (3)

$$D_{XRD} = \frac{K\lambda}{\Delta \cdot \cos\theta} \quad (3)$$

where λ is the wavelength of the Cu $K_{\alpha 1}$ X-ray radiation (1.5406 Å), θ is the diffraction angle, Δ is the width of the peak at half of its maximum and *K* is the constant assumed to be 1 [59]. The error for the crystal size estimation was ~ 5 – 10% depending on the value of the crystal size. The relative gahnite and rutile crystallinity fractions were estimated by the intensity of the gahnite peak with the Miller's indices (311) at 2θ = 36.6° and the intensity of the rutile peak with the indices (110) at 2θ = 27.27°.

All the spectroscopic studies were performed at room temperature. Unpolarized Raman spectra were measured in backscattering geometry using a confocal InVia Renishaw Raman microscope equipped with a ×50 Leica objective (N.A. = 0.75), TE cooled CCD camera and an edge filter. The excitation wavelength was 514 nm (Ar+ ion laser lines). The spectral resolution was 2 cm^{-1}. Every spectrum was averaged over 10 acquisitions with duration of 50 s.

Absorption spectra of the initial glasses, glasses heat-treated at the nucleation stage and transparent GCs were recorded with a Shimadzu UV 3600 spectrophotometer in the spectral range from 250 to 3300 nm with a resolution of 1 nm. We used plane-parallel polished on both sides plates 1 mm in thickness, the same as for recording the Raman spectra. Absorption coefficient α was calculated taking into account reflection losses.

Transmission electron microscopy (TEM) study was carried out on a JEOL TEM-1011 microscope with a point resolution of 0.4 nm and an accelerating voltage of 100 kV for initial glasses, the samples heat-treated at the nucleation stage at 720 °C for 6 h and CGs obtained by the

heat-treatment at the second stage at 1000 °C for 6 h. The samples were crushed and dispersed in ethanol. A drop of thus prepared suspension was applied to a TEM-grid.

Densities of the initial glasses and GCs were determined by the Archimedes method with toluene. The experimental error in density measurements was within ±0.0005 g/cm^3.

The coefficients of thermal expansion of the glasses and GCs were measured on a Linseis L 75 VS 1000 dilatometer. Measurements were carried out on rods with a length of 47 to 50 mm and a square section of 5×5 mm. The samples were heated in the temperature chamber of the dilatometer to a temperature of 330 °C at a heating rate of 5 °C·min^{-1}. The thermal expansion coefficients were determined for the initial glasses, for the glasses subjected to the heat-treatment at the nucleation stage, and GCs obtained by subsequent heat-treatments of these glasses in the temperature range from 950 to 1300 °C. The exact heat-treatment schedules are listed in the Results section. The error in determining coefficients of thermal expansion was ± 2%.

Results

3.1. Phase composition and structure of glasses and GCs

3.1.1 Differential scanning calorimetry studies

Figure 2 shows the DSC curves of the quenched initial ZAS and ZAS$_{ox}$ glasses and the curves of the same glasses heat-treated at the nucleation stage (720 °C for 6 h). The DSC curves of the initial glasses are similar to each other and demonstrate one narrow exothermic peak of high intensity.

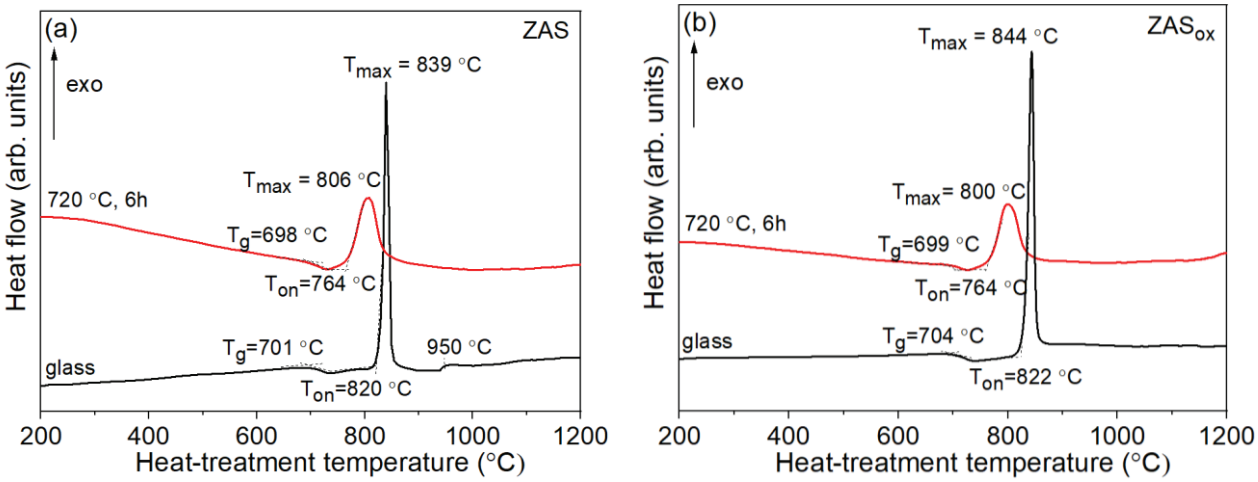

Fig. 2. DSC curves of the quenched initial glasses and glasses heat-treated at 720 °C for 6 h. T_g stands for the glass transition temperature, T_{on} stands for the onset crystallization temperature. (a) ZAS samples; (b) ZAS$_{ox}$ samples. The curves are shifted for the convenience of observation.

The DSC curve of the initial glass melted under normal conditions allows to find the glass transition temperature T_g = 701 °C, the onset crystallization temperature T_{on1} = 820 °C, the crystallization maximum temperature T_{max1} = 839 °C, and the weak exothermal peak with the T_{on}

= 950 °C, see Fig. 2(a) and Table 1. Comparison of the DSC curves of initial ZAS and ZAS_{ox} glasses shows that their characteristic temperatures are near the same, see Table 1, if not to take into account an absence of the weak exothermal peak at 950 °C in the DSC curve of the ZAS glass.

The DSC curves of samples heat-treated at 720 °C for 6 hours are also similar to each other but different from the curves of the initial glasses. After the preliminary heat-treatment, the exothermal peaks becomes broader and appear at temperature lower than those for the initial glasses by about 60 °C, which proves the modification of the structure of initial glasses by this heat-treatment while materials remain X-ray amorphous, see Fig. 3(a,b). This structure modification is further confirmed by Raman and optical spectroscopy data, TEM images, and density measurements of the samples, see below. It is interesting that the T_g temperature does not change with this heat-treatment, see Fig. 2(a,b) and Table 1. It means that the structure modification at the nucleation stage occurs in phase separated amorphous regions and does not change significantly the structure of the residual silicate glass network, see below.

Table 1. Characteristic temperatures derived from the DSC curves of the initial ZAS and ZAS_{ox} glasses and glasses heat-treated at 720 °C for 6 h.

Heat-treatment schedule	ZAS			ZAS_{ox}		
	T_g, °C	T_{on}, °C	T_{max}, °C	T_g, °C	T_{on}, °C	T_{max}, °C
Initial glass	701	820	839	704	822	844
720 °C, 6 h	698	764	806	699	764	800

3.1.2. Study of the phase composition of the initial glasses and glass-ceramics by the X-ray diffraction analysis

Figure 3 shows the evolution of diffraction patterns of ZAS and ZAS_{ox} glasses as a function of the heat-treatment temperature. Initial glasses and glasses heat-treated at the nucleation stage at 720 °C for 6 h are X-ray amorphous. The amorphous halo maximum is located at $2\theta \sim 26.2°$, see Fig. 3(a,b). The samples of ZAS and ZAS_{ox} GCs prepared by the two-stage heat-treatments with the temperature of the second stage from 750 to 950 °C contain gahnite, PDF card #74-1136, as the sole crystal phase. Rutile (TiO_2), PDF card #75-1748, crystallizes additionally at the temperature of the second stage of 1000 °C and above. After heat-treatments in the temperature range from 750 to 1200 °C, the composition of the residual glass gradually approaches that of silica glass by the shape and location, as the position of the maximum of amorphous halo shifts from $2\theta = 26.2°$ to 21.6°, see Fig. 3(a,b). The amorphous halo disappears only with crystallization of cristobalite at high heat-treatment temperatures, Fig. 3(c,d).

In GCs of the ZAS_{ox} composition prepared by the two-stage heat-treatment with the second stage at 1300 °C, the third crystalline phase is found, e.i., SiO_2, α-cristobalite, with space group $P4_12_12$. Figure 3(d) clearly demonstrates the XRD pattern with not only the strongest peak of α-

cristobalite at 2θ = 21,6°, but with a number of peaks with lower intensities. All the main diffraction lines of α-cristobalite with the Miller's indices of (101), (111), (112), (200), (113), and (212) are seen in the pattern. Position of lines with indices of (111) and (113) allowed us to reliably calculate the unit cell parameters of α-cristobalite, see Table 2. Larger parameters and volume of the unit cell of α-cristobalite as compared with literature, see Table 2, may be due to the incorporation of impurities [60] from the residual glass.

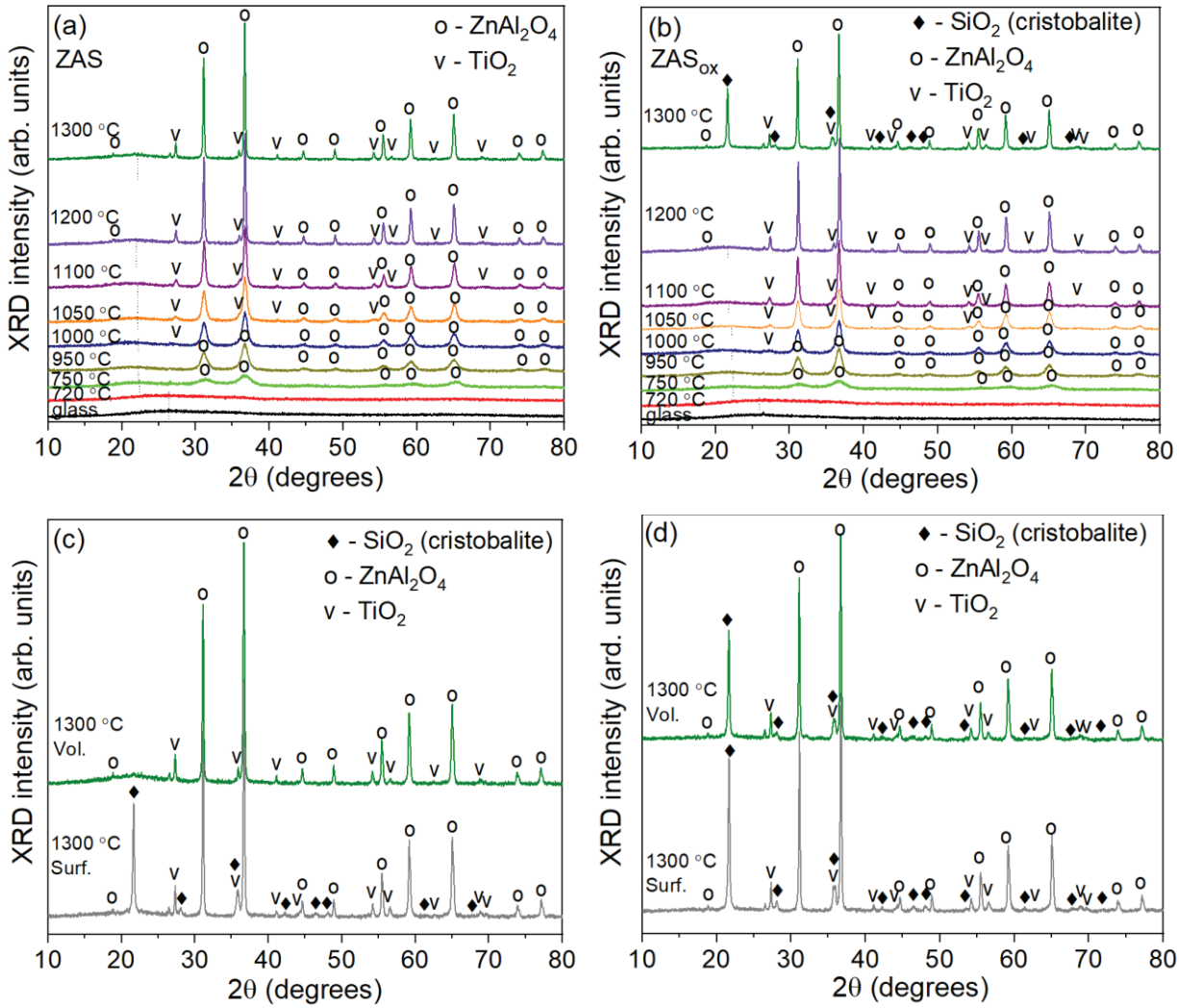

Fig. 3. XRD patterns of initial glasses and glass-ceramics prepared by heat-treatments in the temperature range from 720 to 1300 °C. (a,c) XRD patterns of samples prepared from glasses melted in normal conditions; (b,d) XRD patterns of samples prepared from glasses melted in oxidizing conditions; (c,d) XRD patterns from the surface and the volume of GC prepared by the heat-treatment at 1300 °C. The first stage is at 720 °C. Labels 750–1300 °C indicate the heat-treatment temperature at the second stage. Holding time at each stage is 6 h. Dashed lines in (a,b) indicate position of the maximum of amorphous hallo. The patterns are shifted for the convenience of observation.

Figure 3(c,d) presents XRD patterns of powders made from the surface layer and the volume of GCs prepared by the heat-treatment at the second stage at 1300 °C. Comparison of XRD patterns recorded from the volume and the surface of the ZAS GC shows that crystallization of α-

cristobalite starts from the surface of this sample, see Fig. 3(c). Comparison of powder XRD patterns of the ZAS_{ox} GC prepared from the surface and the volume of the sample, demonstrates that the crystallinity fraction of α-cristobalite is higher on the surface than in the volume of this sample. It can be assumed that appearance of α-cristobalite in the bulk of the ZAS_{ox} sample is due to a more intense surface crystallization of this phase, so that during the heat-treatment time of 6 h, cristobalite crystals grow from the surface into the bulk of this GC. To prove this assumption, the samples were heat-treated at the second stage at 1350 °C. The resulting samples are visually homogeneous, in contrast to the samples obtained by the heat-treatment at 1300 ° C, in which a crust is visible due to the surface crystallization of cristobalite.

Figure 4 confirms that α-cristobalite, which crystallizes from the surface, can be found even in the volume of GCs of the ZAS and the ZAS_{ox} compositions prepared by the heat-treatment at the second stage at 1350 °C. Thus, we confirm the surface crystallization of α-cristobalite from the residual glass in both GCs. This finding is in line with the results presented by G.H. Beall and D.A. Duke [26] for gahnite-based GCs containing ZrO_2 as a nucleating agent. They stated that cristobalite might form through devitrification of the residual siliceous glass, if the GCs are held at temperatures above 1000 °C for several hours. It is nucleated at the air-GC interface and not inside the GC [26].

Table 2. The parameters *a*, *c*, and volume of α-cristobalite unit cell in glass-ceramics and in the standard XRD cards.

Material designation	ZAS	ZAS	ZAS	ZAS_{ox}	ZAS_{ox}	ZAS_{ox}	PDF card #76-0939	PDF card #76-0941	PDF card #82-0512
Heat-treatment	1300 °C surf.	1300 °C vol.	1350 °C vol.	1300 °C surf.	1300 °C vol.	1350 °C vol.	-	-	-
$d_{(101)}$, Å	4.101	-	4.097	4.099	4.103	4.093	4.066	4.073	4.081
a, ± 0.003, Å	5.039	-	5.037	5.033	5.035	5.039	4.993	4.998	4.997
c, ± 0.003, Å	7.003	-	6.994	7.003	7.033	6.982	7.005	7.024	7.070
V, ± 0.1, $Å^3$	177.8	-	177.4	177.4	178.3	177.3	174.7	175.5	176.5

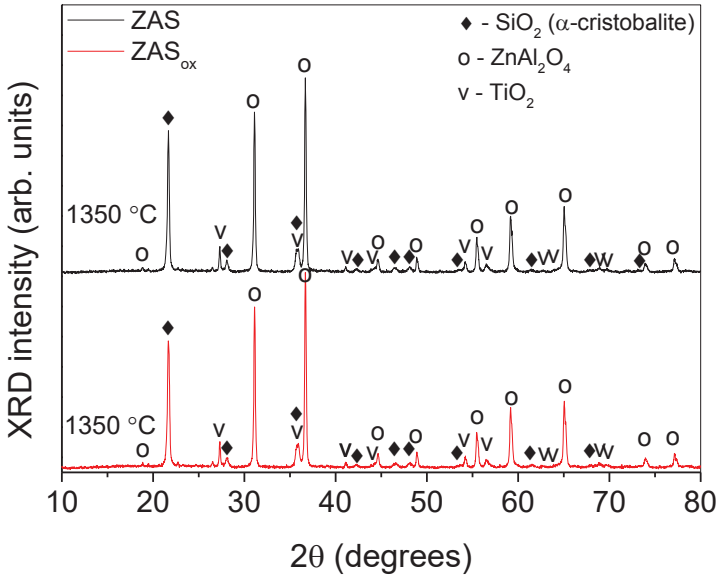

Fig. 4. XRD patterns of glass-ceramics prepared by the heat-treatment at 1350 °C for 6 h. The first stage is 720 °C for 6 h. The patterns are shifted for the convenience of observation.

It is known that cristobalite is stable at high temperatures and low pressures in its cubic β form, and undergoes a spontaneous displacive phase transition to tetragonal α-cristobalite upon cooling [61]. As a result of the β- to α- transition, β-cristobalite is not expected in nature under ambient conditions. The β- to α-cristobalite transition is accompanied by a ~5% reduction in volume, which causes the crystals to crack on cooling [60]. We did not perform the *in situ* high-temperature XRD study of GCs prepared at 1300 – 1350 °C upon their cooling and were not able to detect the β- to α-cristobalite phase transition. We believe α-cristobalite is formed in our GCs from β-cristobalite upon cooling, which is indirectly confirmed by cracks formation in GCs.

Figure 5 shows variation of intensity of the gahnite peak with the Miller's indices (311) and of the average size of gahnite crystals with the heat-treatment temperature for glasses melted in different conditions. The redox conditions of glass melting do not influence these parameters. In the heat-treatment temperature range from 750 to 1050 °C, intensity of the gahnite peak, which is the measure of the gahnite crystallinity fraction, increased approximately linearly. As the temperature increases from 1100 to 1350 °C, the rate of increase in the gahnite crystallinity fraction rapidly grows.

Heat-treatment clearly increases the size of the nanocrystals as demonstrated by the decrease in peaks broadening, see Fig. 3(a,b). Figure 5(b) and Table 2 reveal that the gahnite crystal size increases near twice, from 6 to 11 nm as the heat-treatment temperature at the second stage rises from 750 to 1000 °C. The obtained GCs are transparent, see Fig. 1. The crystal size rapidly increases more than 5 times, from 15 to 50 nm, when the heat-treatment temperature at the

second stage increases from 1050 to 1350 °C. Figure 1 shows that the GCs become translucent and then, opaque.

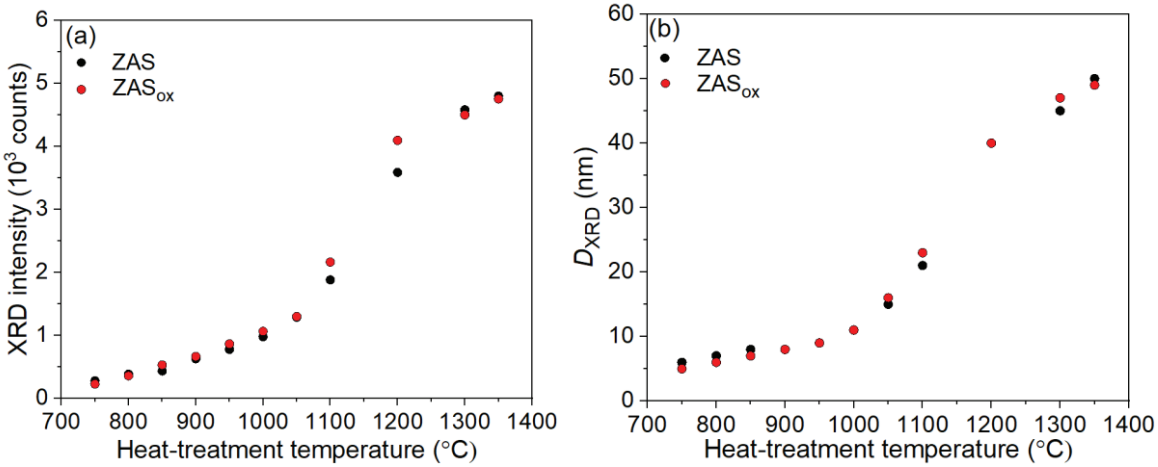

Fig. 5. Intensity of the gahnite peak with Miller's indices (311) and average gahnite crystal size as functions of the heat-treatment temperature of the initial glass. The heat-treatment at the nucleation stage is 720 °C for 6 h. The holding time at the second stage is 6 h.

The values of the parameter *a* of the gahnite unit cell in GCs of the ZAS and ZAS$_{ox}$ compositions prepared at different heat-treatment temperatures are presented in Fig. 6 and in Table 3. According to the literature data (PDF card #74-1136), the gahnite unit cell parameter is 8.086 Å. At the beginning of the gahnite crystallization at 750 °C its structure corresponds to a normal spinel with a low degree of inversion [15]. An increase of the heat-treatment temperature up to 850 °C leads to appreciable increase of the unit cell parameter *a*, which takes the value of 8.109 Å for the ZAS GC and of 8.111 Å for that of the ZAS$_{ox}$. At further increase in the heat-treatment temperature, even greater values of parameter *a* of up to 8.113 Å are observed. They do not change significantly up to the heat-treatment temperature of 1350 °C. The values of the unit cell parameter *a* and their dependence on the heat-treatment temperature are similar for the ZAS and ZAS$_{ox}$ GCs.

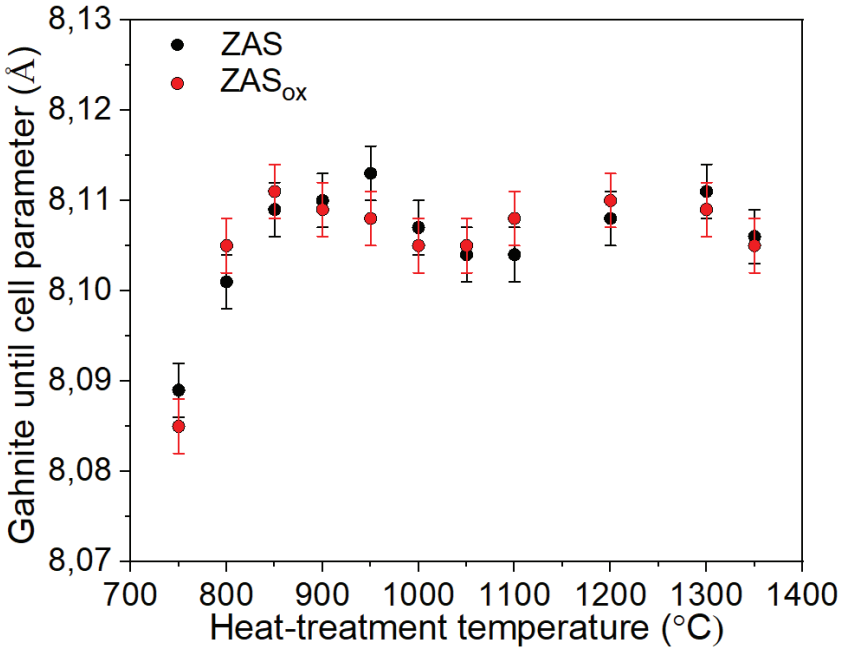

Fig. 6. The gahnite unit cell parameter *a* as a function of heat-treatment temperature of initial glasses. The heat-treatment at the nucleation stage is 720 °C for 6 h. The holding time at the second stage is 6 h.

Table 3. The unit cell parameters of gahnite and rutile nanocrystals, and their average sizes

Heat-treatment schedule	ZAS					ZAS_{ox}				
	$ZnAl_2O_4$		TiO_2 (rutile)			$ZnAl_2O_4$		TiO_2 (rutile)		
°C/ 6 h	*a*, ± 0.003, Å	*D*, nm	*a*, ± 0.003, Å	*c*, ± 0.003, Å	*D*, nm	*a*, ± 0.003, Å	*D*, nm	*a* ± 0.003, Å	*c* ± 0.003, Å	*D*, nm
initial glass	-	-	-	-	-	-	-	-	-	-
720	-	-	-	-	-	-	-	-	-	-
720+750	8.089	6	-	-	-	8.085	5	-	-	-
720+800	8.101	7	-	-	-	8.105	6	-	-	-
720+850	8.109	8	-	-	-	8.111	7	-	-	-
720+900	8.110	8	-	-	-	8.109	8	-	-	-
720+950	8.112	9	-	-	-	8.108	9	-	-	-
720+1000	8.107	11	-	-	12	8.105	11	-	-	11
720+1050	8.104	15	4.618	2.950	15	8.105	16	4.613	2.959	14
720+1100	8.104	21	4.621	2.949	21	8.108	23	4.611	2.961	24
720+1200	8.108	39	4.618	2.952	37	8.110	40	4.611	2.957	38
720+1300	8.111	45	4.619	2.949	50	8.109	47	4.612	2.955	51
720+1350	8.106	50	4.619	2.949	55	8.105	49	4.613	2.958	51

Figure 7 shows dependences of intensity of the rutile peak with the Miller's indices (110) and of the average size of rutile crystals on the heat-treatment temperature in GCs with compositions ZAS and ZAS_{ox} in the temperature range from 1000 to 1350 °C. The crystallinity fraction and size of rutile crystals rise with increasing the heat-treatment temperature in the range of 1000 – 1300 °C for GCs of both compositions (see Table 3). There is a rapid increase in the rutile crystallinity fraction in the ZAS_{ox} GC prepared at 1200 °C, which we did not take into account while drawing the straight line as a guide for an eye. The average crystal size of rutile in GCs of both compositions increases from ~11 nm to ~50 nm with increasing the heat-treatment

temperature in the range from 1000 to 1350 °C. The crystal sizes of rutile are very similar in GCs of both compositions.

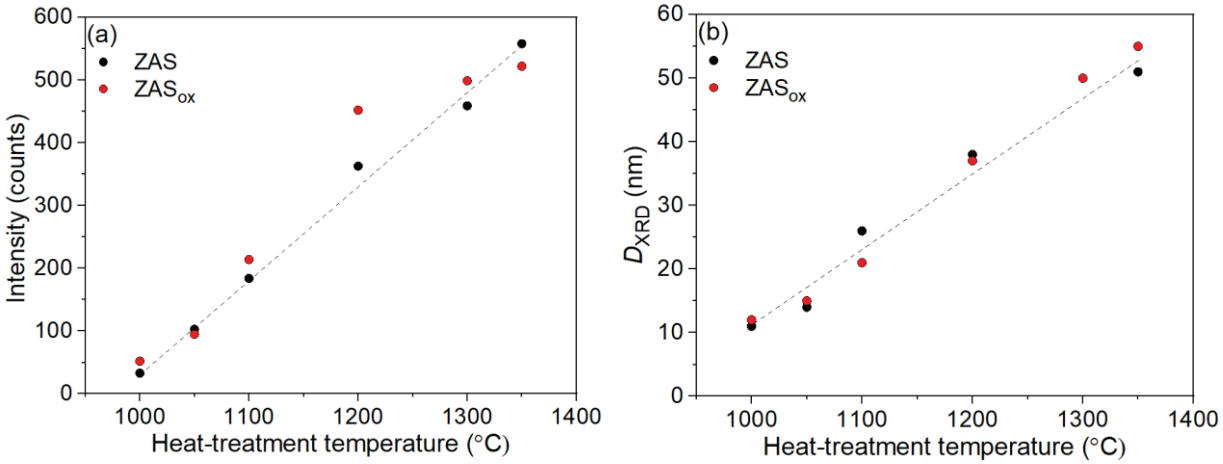

Fig. 7. (a) Intensity of the rutile (TiO_2) peak with Miller's indices (110) and (b) average rutile crystal size as a function of heat-treatment temperature of initial glasses of the ZAS and ZAS_{ox} compositions. The heat-treatment at the nucleation stage is 720 °C for 6 h. The holding time at the second stage is 6 h. The lines are guides for an eye.

The rutile unite cell parameters *a* and *c* in GCs prepared by heat-treatments in the temperature range from 1050 to 1350 °C are shown in Fig. 8 and in Table 2. The unit cell parameters of rutile depend on the composition of GCs while they are independent of the heat-treatment temperature. The average rutile unit cell parameters *a* and *c* in GCs of the ZAS composition are $a = 4.619 \pm 0.003$ Å and $c = 2.950 \pm 0.003$ Å; in GCs of the ZAS_{ox} composition the rutile parameters $a = 4.612 \pm 0.003$ Å and $c = 2.958 \pm 0.003$ Å, see Table 2 and Fig. 8(a,b). It means that the glass melting redox conditions influence the structure of rutile crystallized during the high-temperature heat-treatments. The rutile parameter *a* in the ZAS GCs is larger than in the ZAS_{ox} one, while the *c* parameter is smaller. The differences in the values of these parameters indicate a different degree of distortion of the (TiO_6) octahedrons building the rutile structure of these GCs. It can be assumed that this difference is caused by the presence of Ti^{3+} ions in the rutile octahedrons in ZAS GCs. Differences of rutile unit cell parameters in ZAS and ZAS_{ox} GCs are preserved at increasing of heat-treatment temperature. Despite these differences, the unit cell volume of rutile crystals in ZAS and ZAS_{ox} GCs is similar. It is equal to 62.94 ± 0.01 Å^3 and 62.92 ± 0.01 Å^3 for the ZAS and the ZAS_{ox} GCs, respectively and testifies to distortion structural changes that occur in rutile octahedrons without bond breaking.

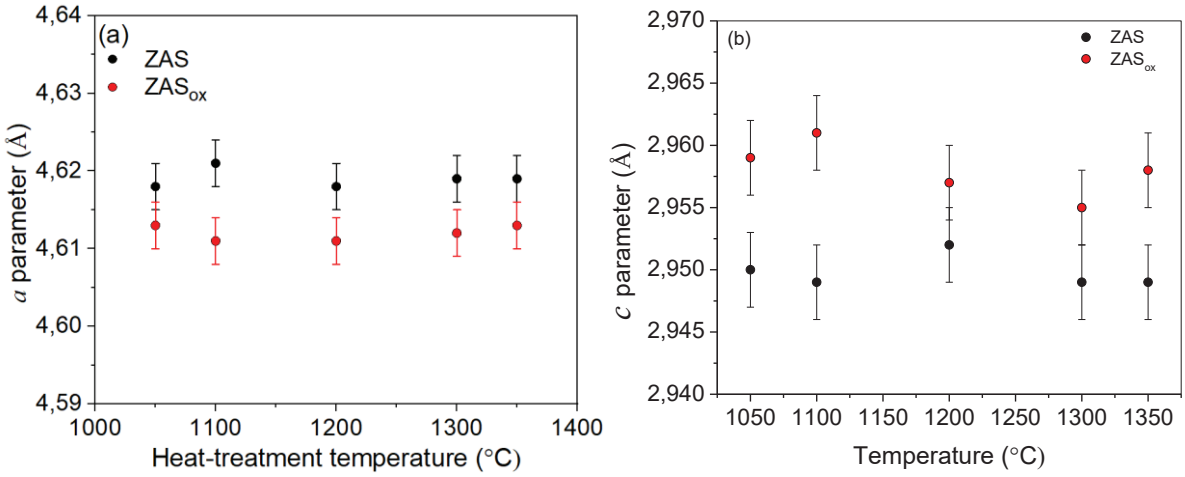

Fig. 8. Rutile unit cell parameters (a) *a* and (b) *c* as a function of the heat-treatment temperature of the initial glasses of the ZAS and ZAS_{ox} compositions. The heat-treatment at the nucleation stage is 720 °C for 6 h. The holding time at the second stage is 6 h.

3.1.3. Raman spectroscopy

Figure 9(a,b) presents Raman spectra of initial ZAS and ZAS_{ox} glasses, glasses heat-treated at the nucleation stage at 720 °C for 6 h and GCs prepared by the two-stage heat-treatments with the second stage in the temperature range from 750 °C to 1200 °C. With the aim to follow the details of amorphous phase separation of titanium-containing phases [32] and beginning of crystallization, Fig. 9(c,d) presents Raman spectra of ZAS and ZAS_{ox} initial glasses, glasses heat-treated at the nucleation stage at 720 °C for 6 h and GCs prepared by the two-stage heat-treatments with the second stage in the temperature range from 750 °C to 1000 °C. The spectra of both initial glasses heat-treated at the nucleation stage at 720 °C are presented in Fig. 9(e), while the spectra of glasses heat-treated at 850 °C, 950 °C, and 1200 °C at the second stage are shown in Figs 9(f-h) for comparison.

The Raman spectrum of the initial glass of the ZAS composition contains a broad band of low intensity spanning from ~220 to ~520 cm^{-1} with a band at ~460 cm^{-1} and two maxima on the low-frequency side of this band, near ~270 and ~380 cm^{-1} [32,62], and two bands in the high-frequency region at ~800 and ~930 cm^{-1}, see Fig. 9(a,c). The bands at ~460 and ~800 cm^{-1} are assigned to vibrations of aluminosilicate tetrahedra in the glass structure while the band at ~ 930 cm^{-1} is connected with the presence of $[TiO_4]$ tetrahedra entered into this aluminosilicate network [32 and references therein, 63].

Figure 9(c) shows that after the heat-treatment of the ZAS glass at 720 °C for 6 h the spectrum changes: the band at ~460 cm^{-1} shifts to ~450 cm^{-1}, and a high-frequency band shifts from ~930 to ~920 cm^{-1}. After this heat-treatment, a slight redistribution of the intensities of the two bands in the high-frequency region is seen as compared with intensities distribution in the initial glass. Intensity of the band at ~800 cm^{-1} slightly enhances, manifesting the development of

liquid phase separation of the initial glass with the formation of the zinc aluminotitanate amorphous phase [32].

After the two-stage heat-treatment with the second stage at 750 °C, the band previously located at about 450 cm^{-1} shifts to 440 cm^{-1}, which corresponds to the position of the main band in the silica glass [64]. Two weak bands appear at ~489 and 602 cm^{-1}. They are the so-called defect bands D_1 and D_2 [64-66] assigned by Galeener [65] to 'breathing' vibration modes of four- and three-membered rings, respectively, in the silica glass. Thus, the data of Raman spectroscopy confirm that as a result of heat-treatment the composition of the residual glass becomes close to silica glass. These spectral features are in accordance with the shift of the amorphous hallo position in the XRD pattern of this GC to that of silica glass, see Fig. 3(a). The weak band at about 800 cm^{-1}, corresponding to vibrations of the aluminosilicate network, is superimposed over the intense band at ~790 cm^{-1}, associated with vibrations of [TiO_5] and [TiO_6] groupings [32], while the band at about ~920 cm^{-1} near disappears. This is the result of the liquid phase separation of the glass with the formation of the amorphous zinc aluminotitanate phase, whose spectral feature is the broad band at ~790 cm^{-1} [32].

According to the XRD data, Fig. 3(a), gahnite crystals appear during the heat-treatment at 750 °C. It is known that five active modes $A_{1g} + E_g + 3F_{2g}$ should be observed in the Raman spectra of normal spinels [67-71]. Their wavenumbers are in the following sequence, $F_{2g}(1) < E_g < F_{2g}(2) < F_{2g}(3) < A_{1g}$. [68]. According to Refs [69,70], in the Raman spectrum of gahnite, the low-frequency $F_{2g}(1)$ mode (196 cm^{-1}) is assigned to a complete translation of the ZnO_4 within the spinel structure, while the phonon modes with higher frequencies are due to O and Al, with a major contribution of O than Al; the frequencies over 729 cm^{-1} are predominantly due to O motions. The disordering can cause a breakdown in the Raman selection rules; the inversion degrees cause the appearance of an additional peak at ~700 – 730 cm^{-1} attributed to A_{1g} character and assigned to the Al-O stretching vibration of AlO_4 groups created by redistribution of some aluminum ions from octahedral to tetrahedral sites [71].

The positions of Raman modes of gahnite nanocrystals in GC of the composition similar to studied here were determined in Ref. [24]. They were the T_{2g} (196 cm^{-1}), E_g (~420 cm^{-1}), T_{2g} (659 cm^{-1}) and A_{1g} (~780 cm^{-1}) modes. The broad intense asymmetric band with an inflection at ~720 cm^{-1} and a maximum at ~780 cm^{-1} was assigned to entering the titanium ions into gahnite crystals in octahedral positions [72,73].

Thus, we suggest that weak bands with frequencies of ~418 and ~657 cm^{-1} in the Raman spectrum of GC prepared by the heat-treatment with the second stage at 750 °C belong to E_g and T_{2g} modes in gahnite crystals, respectively [32,56]. There is also an inflection on the left side of the broad high-frequency band at ~732 cm^{-1}. In Refs [72,73] the appearance of a similar band was

assigned to breaking of the symmetry selection rules caused by doping gahnite crystals with Ti^{4+} ions. The ZAS GC contains both Ti^{4+} and Ti^{3+} ions. We suggest that in the ZAS GC the band at ~732 cm^{-1} is also connected with titanium doping of nanocrystalline $ZnAl_2O_4$.

In the Raman spectrum of GC prepared by the heat-treatment at the second stage at 800 °C, one intense band ~790 cm^{-1} with inflection at ~732 cm^{-1}remains in the high-frequency region of the spectrum. It is comparable in intensity to the band ~440 cm^{-1}, a characteristic band of the highly siliceous residual glass. Two weak bands at ~418 and ~657 cm^{-1} and inflection at ~732 cm^{-1} belong to vibrations in the $ZnAl_2O_4$ gahnite crystals, as mentioned above. A weak band at ~144 cm^{-1} appears in the region of lower wavenumbers. It corresponds to the strongest band in the Raman spectrum of anatase [32], a modification of TiO_2. Increasing the heat-treatment temperature to 1000 °C and above leads to an appearance of new bands, i.e., a weak composite peak at 235 cm^{-1}, a narrow maximum at ~440 cm^{-1} located on the wide band of the residual glass and a band at ~606 cm^{-1}. They correspond to vibrations in the TiO_2 rutile crystals [74,75] and confirm the findings of the XRD analysis, Fig. 3(a). With a further increase in the heat-treatment temperature up to 1200 °C, intensities of the gahnite and rutile bands increase, and the broad band at 790 cm^{-1} gradually weakens. In the Raman spectrum of GC prepared at 1200 °C, on the background of an increased rutile band of 440 cm^{-1}, a weaker band of gahnite at 418 cm^{-1} becomes poorly resolved.

Two weak bands at ~940 and ~1108 cm^{-1} are seen in the high-frequency region of Raman spectra of GCs prepared by heat-treatments at temperatures from 800 °C to 1200 °C. They are associated with vibrational modes of isolated titanium centers in the highly siliceous residual glass phase [32]. After heat-treatments at 1100 and 1200 °C, the spectra of the samples show a band at about 705 cm^{-1}, which can be caused by inversion of gahnite crystal structure [24,76]. In the spectrum of the sample obtained after heat-treatment at 1200 °C, a weak band with a maximum ~800 cm^{-1} is observed, which is also assigned to gahnite [24].

The Raman spectra of the ZAS_{ox} glass and GCs are similar to spectra of the ZAS samples, see Fig. 9(b,d). However, there is a slight difference in the position of some broad bands, which sometimes reaches 10 cm^{-1} (920 cm^{-1} instead of 930 cm^{-1} for the initial glass and 790 cm^{-1} instead of 780 cm^{-1} for GCs prepared at 850-950 °C).

For a detailed comparison of the behavior of glasses obtained under different redox conditions, the spectra of samples heat-treated at the nucleation stage of 720 °C are shown in Fig. 9(e). In the Raman spectrum of the glass of the ZAS_{ox} composition that has undergone the preliminary heat-treatment at the nucleation stage of 720 °C, the high frequency band is located at ~900 cm^{-1} instead of ~920 cm^{-1} (position in the spectrum of the ZAS sample). In the spectrum of the ZAS sample, the band at 800 cm^{-1} is lower in intensity than the band at ~920 cm^{-1}, while in the spectrum of the ZAS_{ox} samples intensities of these neighbor bands are near equal. Enhancement

of the peak at about 800 cm^{-1} in the spectrum of the ZAS_{ox} glass after its heat-treatment at 720 °C proves that oxidation melting conditions speed up the liquid phase separation in the initial glass.

Figures 9(f,g) show that the spectral features of rutile crystallization appeared in the Raman spectrum of the ZAS_{ox} subjected to the heat-treatment at 850 °C while in the ZAS GC prepared by this heat-treatment and even by the heat-treatment at 950 °C rutile features are not seen. Thus, we may conclude that glass melting in oxidizing conditions speeds up rutile crystallization. It should be noted that Raman spectroscopy is more sensitive to phase transformations of titanium-containing phases, then the XRD analysis, see Fig. 3(b), and allows to see the spectral features of structural ordering in the zinc aluminotitanate amorphous regions in GCs whose XRD patterns do not show rutile crystallization yet.

Intensities of the gahnite and rutile bands in the Raman spectrum of the ZAS_{ox} GC prepared by the heat-treatment at 1200 °C are higher than in the spectrum of the ZAS one, see Fig. 9(h). This observation is confirmed by the XRD data, see Figs 5(a) and 7(a). Thus, we can conclude that according to the Raman spectroscopy data, the ZAS_{ox} glass melting in oxidizing conditions speeds up the liquid phase separation of the initial glass and rutile crystallization.

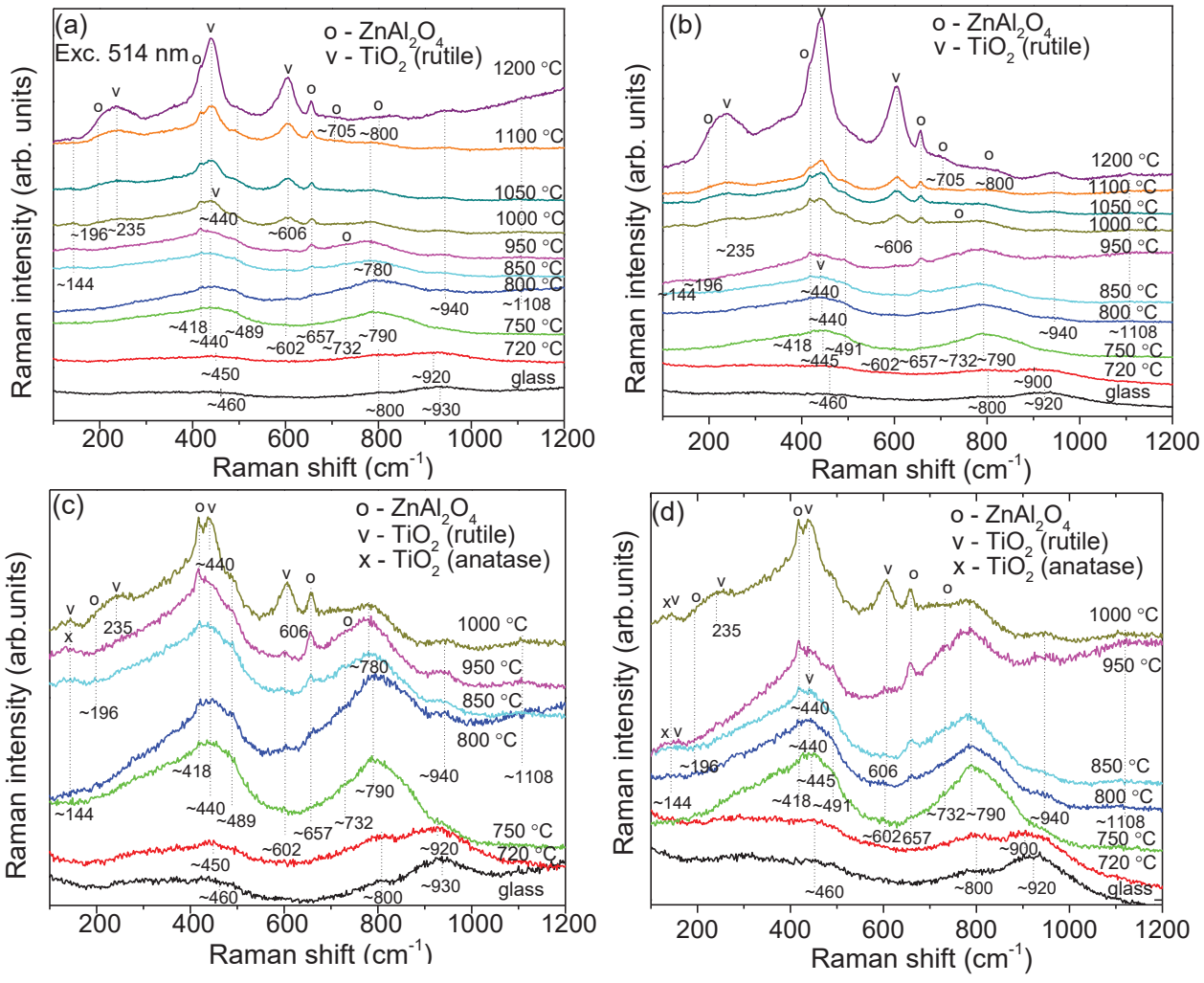

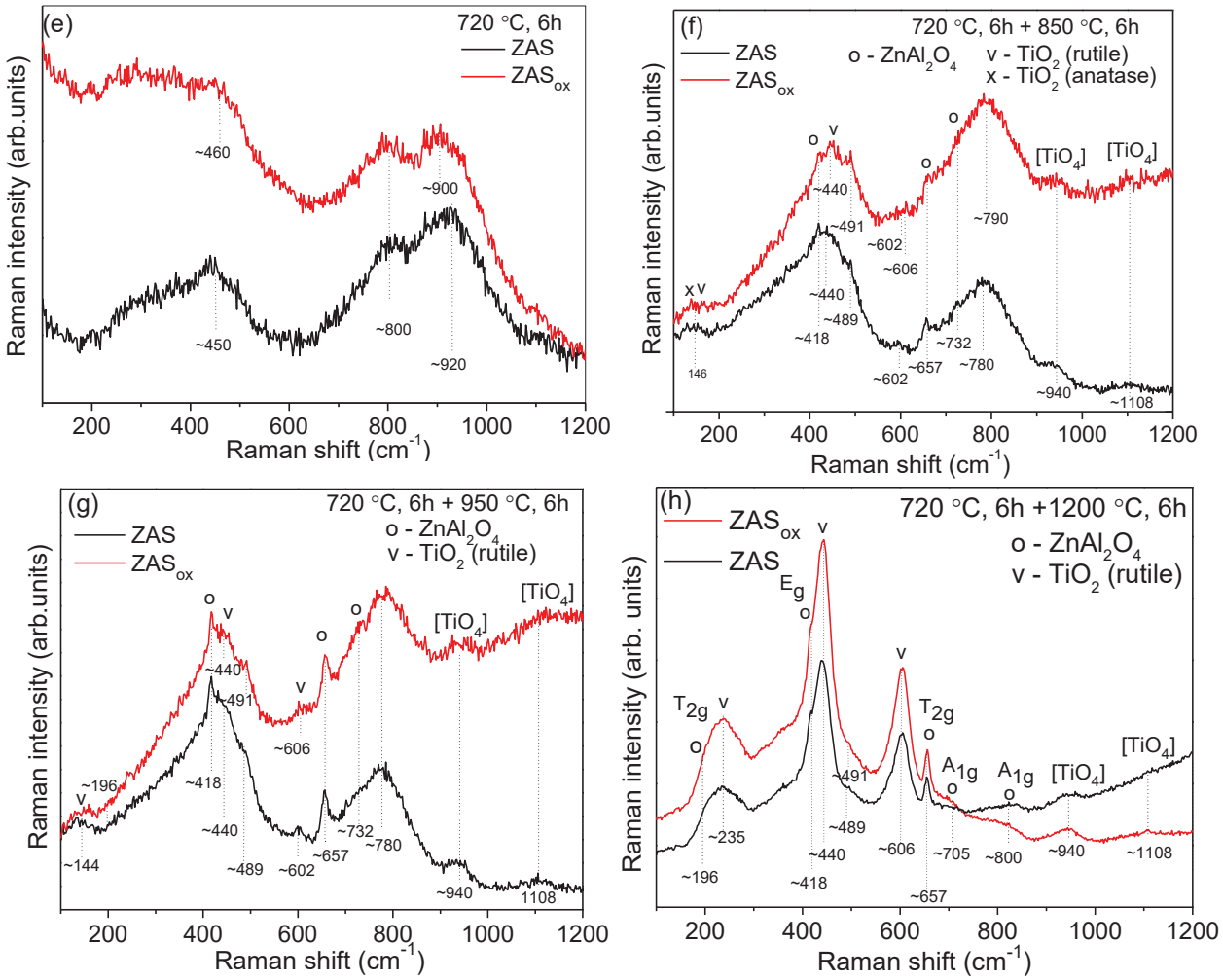

Fig. 9. Raman spectra of initial glasses and glass-ceramics prepared by heat-treatments in the temperature range from 720 °C to 1200 °C. (a,c) Spectra of samples prepared from glasses melted in normal conditions; (b,d) Spectra of samples prepared from glasses melted in oxidizing conditions; (e) Spectra of samples obtained by the heat-treatment at 720 °C; (f) Spectra of samples obtained by the heat-treatment at 720 °C + 850 °C; (g) Spectra of samples obtained by the heat-treatment at 720 °C + 950 °C. (h) Raman spectra of samples obtained by the heat-treatment at 720 °C + 1200 °C The holding time is 6 h. The spectra are shifted for the convenience of observation. λ_{excit} = 514 nm.

3.1.4. Transmission electron microscopy

Figure 10, which presents typical TEM images of the initial glasses, the glasses after the nucleation heat-treatment and the GCs prepared by the two-stage heat-treatment with the second hold at 1000 °C for 6 h, allows to follow the variation of the microstructure with heat-treatment. Figure 10(a,d) shows the phase separation in the annealed glasses. The average size of amorphous inhomogeneous regions is ~5 nm. According to small-angle X-ray scattering findings [32], these are the zinc aluminotitanate amorphous regions that predominantly precipitate upon casting, cooling and annealing the glasses. There is certain regularity in their distribution within the initial glasses, which is preserved even after further heat-treatments [32]. Figure 10(b,e) shows that the inhomogeneous regions develop in both glasses after the nucleation heat-treatment at 720 °C. Their

average sizes are ~7 nm and ~6 nm for the ZAS and ZAS_{ox} samples, respectively. Note that the XRD patterns of these samples indicate the lack of any crystalline phase, while the findings of small-angle X-ray scattering [32] reveal the continued development of zinc aluminotitanate amorphous regions and rapid formation of zinc aluminate amorphous regions.

Figure 3(a,b) shows that according to XRD data, crystallization of gahnite starts at 750 °C, and at 1000 °C the number of gahnite crystals increases significantly accompanied by the rutile crystallization. The TEM images of GCs obtained by the heat-treatment with the second hold at 1000 °C reveal the multiphase nature of these GCs. They present well-faceted crystals of different shapes. In TEM images, gahnite crystals appear as grey, sometimes almost black particles. Most of these particles have an isometric shape with facets. Moreover, some particles have an octahedral shape. The octahedron is a typical form of spinel. Dark particles that have different shapes are intergrowths of two or more octahedrons. The formation of such intergrowths is characteristic of gahnite crystals. Cut shapes of rutile crystals are tetragonal prism and bipyramid. It is possible to assume that the elongated rectangular shaped particles are rutile crystals. The average crystal sizes of spinel and rutile crystals estimated from the TEM images appear to be similar. They are ~16 nm for both GCs. These crystal sizes are somewhat larger than those determined from the gahnite and rutile XRD peaks broadening, see Table 3. According to Table 3, in the ZAS GC the gahnite and rutile sizes are 11 nm and 12 nm, respectively. In the ZAS_{ox} GC, the gahnite and rutile crystals have similar sizes equal to 11 nm, see Table 3. Probably, the increased crystal size determined from the TEM images is connected with intergrowth of some gahnite crystals.

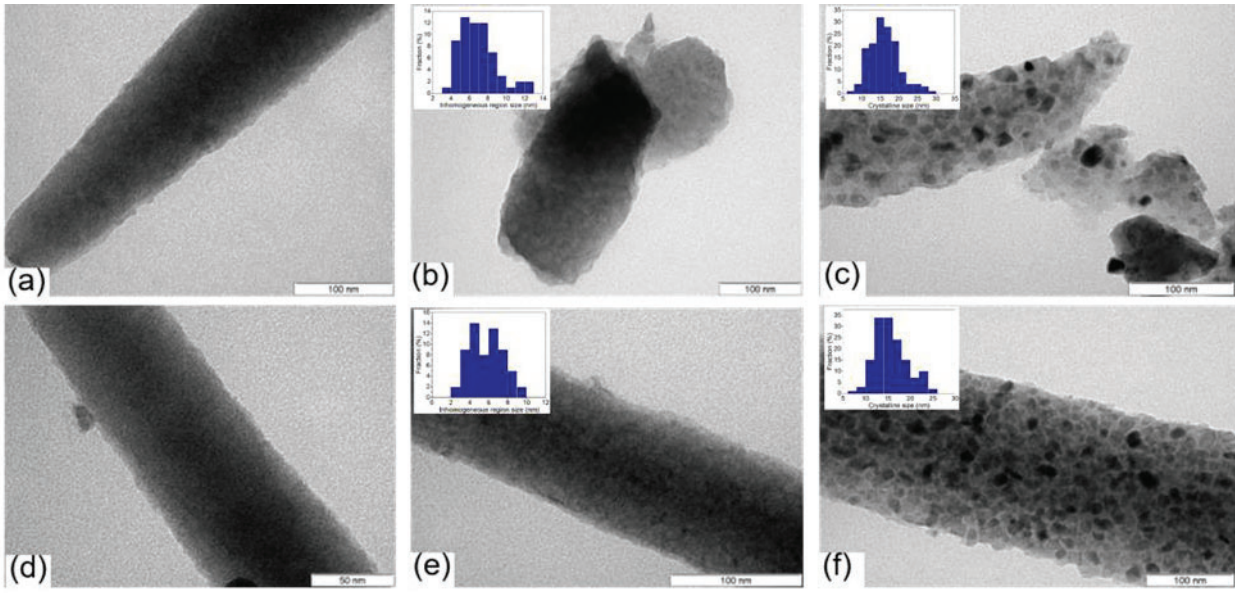

Fig. 10. TEM images of the ZAS (a-c) and ZAS_{ox} (d-f) samples; (a,d) - initial glasses, (b,e) - glasses subjected to the heat-treatment at 720 °C for 6 h, and (c,f) – glass-ceramic prepared by the two-stage heat-treatment with the second hold at 1000 °C for 6 h. Insets present the particle size distributions calculated from TEM data.

3.1.5. Density

Figure 11 shows the variation of the density with heat-treatment of the initial glasses. The density of the ZAS glass is equal to 2.979 g/cm^3. After the heat-treatment at 720 °C it slightly increases to 3.004 g/cm^3, and after the heat-treatment at 750 °C at the second stage the density increases to 3.138 g/cm^3. After further heat-treatments in the temperature range from 800 °C to 1200 °C, the density changes insignificantly, being in the range from 3.119 g/cm^3 to 3.144 g/cm^3.

The density of the glass and GCs of the ZAS_{ox} composition is somewhat higher than the density of the materials of the ZAS composition, while it changes with the heat-treatment temperature in a similar way, varying in details. The initial glass has the density of 3.000 g/cm^3. After the heat-treatment at the nucleation stage, the density slightly increases to 3.020 g/cm^3, and after the heat-treatment at 750 °C at the second stage, it reaches the maximum value of 3.167 g/cm^3. After further heat-treatments in the temperature range from 800 to 1200 °C, the density slightly decreases reaching the value of 3.149 g/cm^3. The densities of the ZAS and the ZAS_{ox} GCs prepared at 1300 °C and 1350 °C could not be measured due to their cracking during these heat-treatments caused by the β- to α-cristobalite phase transition.

It should be noted that GCs, in which the gahnite crystallinity fraction is small because their crystallization has just begun, demonstrate the maximum density, see Fig. 3(a,b). These GCs are characterized by practically completed liquid phase separation and an achievement of relatively steady state of the structure [32]. The fraction of the zinc aluminotitanate phase in these GCs is large, see Fig. 9(a–d), and the residual glass phase composition is already similar to that of the silica glass, see Fig. 3(a,b). Thus, one may conclude that GCs with low gahnite crystallinity fraction but with accomplished liquid phase separation have near the highest density. Despite the increase in the fraction of gahnite with the theoretical density of 4.58 g/cm^3 (obtained from the database ICSD 74-1138) and the crystallization of rutile with the density of about 4,23 – 4,25 g/cm^3 at further heat-treatments, the material density does not grow. It can be explained by the change in the composition of the surrounding residual glass during the crystallization of gahnite and then rutile. Simultaneously with crystallization of the dense gahnite phase and continuing formation of the dense amorphous zinc aluminotitanate phase, wherein rutile crystallizes, a lighter amorphous high-silicate residual glass is formed, the composition of which gradually approaches the composition of silica glass. Note that the density of silica glass is ~2,201 g/cm^3. The combination of dense phases of smaller volumes with a lighter phase of large volume leads to a very insignificant change in the density.

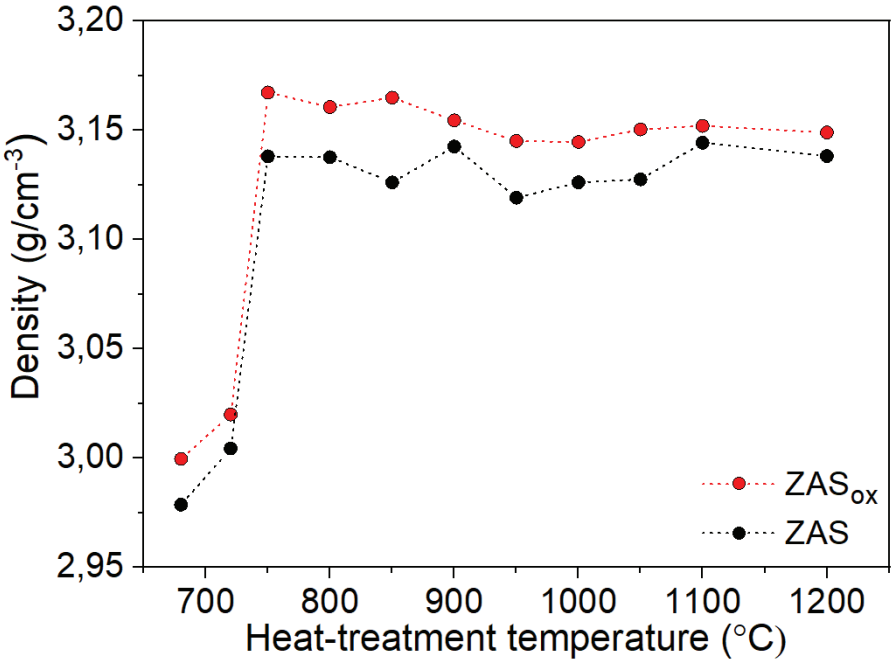

Fig. 11. Variation of the density with heat-treatment temperature for the ZAS and ZAS_{ox} samples. Heat-treatment at the first stage is 720 °C for the samples heat-treated at the second stage in the range from 750 to 1200 °C. The heat-treatment duration at each stage is 6 h. The lines are guides for an eye. Error bars match the size of symbols.

3.1.6. Linear coefficients of thermal expansion

Table 4 gives a summary of thermal expansion coefficients of the initial glasses and GCs in the temperature range from 20 ºC to 320 ºC. It can be seen that both glasses have very similar expansion coefficients of ~3.0×10^{-6} K^{-1}.

The glasses heat-treated at the nucleation stage of 720 °C for 6 h have thermal expansion coefficients slightly increased to $(3.2 - 3.4)\times10^{-6}$ K^{-1}. The GCs prepared by consequent heat-treatments in the temperature range from 950 °C to 1200 °C have thermal expansion coefficients of ~4.5×10^{-6} K^{-1}. The increase in the expansion is due to the growth of gahnite crystals, gahnite having an expansion coefficient of approximately 7.0×10^{-6} K^{-1} (~7.1×10^{-6} K^{-1} according to Ref. [77], or ~6.8×10^{-6} K^{-1} according to Ref. [2]. L. Pinckney mentioned [29] that such a range of thermal expansion matches the thermal expansion of silicon, recommending similar materials as substrates for the active matrix in liquid crystal displays and for integrated circuit packaging. It is interesting that thermal expansion coefficients are near constant for GCs prepared by heat-treatments in the temperature range from 950 °C to 1200 °C. It seems to contradict to a rapid increase of the gahnite crystallinity fraction with increasing the heat-treatment temperature and rutile crystallization, see Fig. 12. Note that rutile has an expansion coefficient of 6.99953×10^{-6} K^{-1} along the *a* axis and 9.36625×10^{-6} K^{-1} along the *c* axis [78]. We believe, the multiphase compositions of these GCs and especially extremely low thermal expansion coefficient of the residual silica-like glass are responsible for the constancy of thermal expansion of GCs. Silica

glass has an expansion coefficient of 0.5 × 10^{-6} K^{-1}. As it was mentioned above, according to the Raman spectroscopy data, highly siliceous silica-like residual glass contains titanium centers. It is well known that titanium-doped silica glass demonstrates extremely low, even zero expansion at room temperature [79,80]. As soon as α-cristobalite is detected in GCs prepared at 1300 °C, see Fig. 12, the thermal expansion coefficient sharply raises to ~21.0×10^{-6} K^{-1}. This raise is explained by the high value of the thermal expansion for α-cristobalite [81]. The thermal expansion coefficients of ~21.0×10^{-6} K^{-1} in the α-cristobalite containing ZAS and ZAS_{ox} GCs are similar to those obtained by A. Hunger *et al.* [82], 20.0×10^{-6} K^{-1}, the largest reported in the literature for alkali-free silicate glass–ceramics.

The thermal expansion coefficients of initial glasses and GCs prepared by heat-treatments in the temperature range from 720 °C to 1300 °C are independent of the redox conditions of glass melting. They depend only on the heat-treatment temperature, which determines the phase composition of the GCs.

Table 4. The thermal expansion coefficients (CTE) in the temperature range from 20 to 320 ºC for the initial glasses, glasses heat-treated at 720 °C for 6 h and GCs prepared by consequent heat-treatments at the second stage in the range from 950 to 1200 °C for 6 h.

Heat-treatment schedule, °C for 6 h	ZAS	ZAS_{ox}
	CTE_{20-330} (×10^{-6} K^{-}	CTE (×10^{-6} K^{-1})
Initial glass	3.00 ± 0.06	3.10± 0.06
720	3.20 ± 0.06	3.40 ± 0.07
720+950	4.50 ± 0.09	4.50± 0.09
720+950+1050	4.50± 0.09	4.60± 0.09
720+950+1050+1200	4.20± 0.08	4.60± 0.09
720+950+1050+1200+1300	20.80 ± 0.42	21.40± 0.43

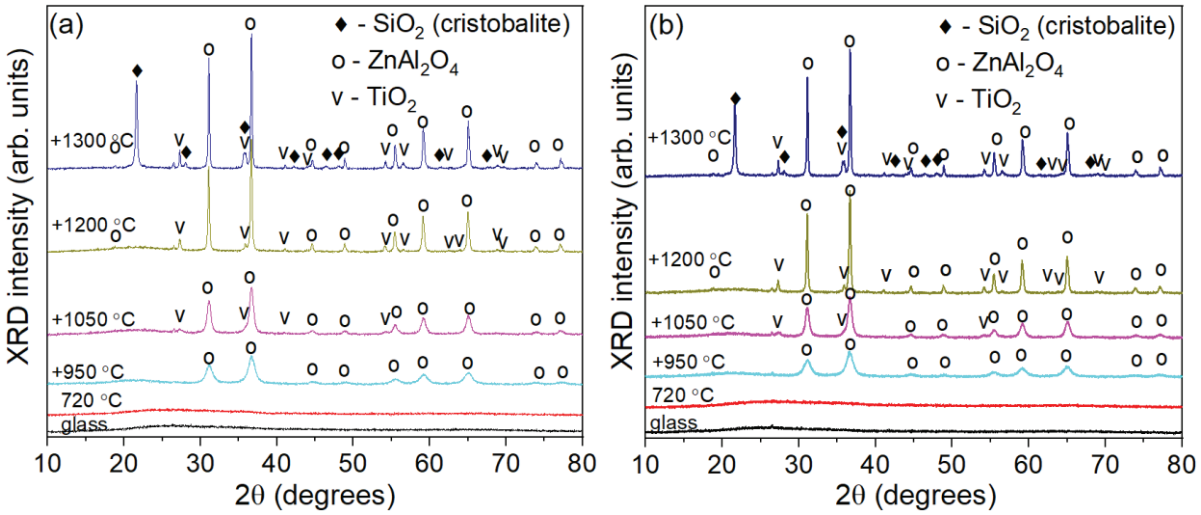

Fig. 12. XRD patterns of initial glasses, glasses heat-treated at 720 °C for 6 h and glass-ceramics prepared by consequent heat-treatments at the second stage in the range from 950 °C to 1200 °C. The heat-treatment at the first stage is 720 °C. The time of heat-treatment at each stage is 6 h.

3.1.7. Absorption spectra

Figure 13 presents absorption spectra of initial glasses, glasses heat-treated at 720 °C, and transparent GCs, prepared by two-stage heat-treatments with temperature from 750 °C to 1050 °C at the second stage. Absorption spectra of the ZAS and ZAS_{ox} samples are quite different, see Fig. 13(a,b), which was expected from their appearance, see Fig. 1.

The data on positions and assignment of absorption bands due to Ti^{3+} and Ti^{4+} ions in glasses can be summarized as follows [83]. Titanium ions are found in glasses in two oxidation states of Ti^{3+} ($3d^1$) and Ti^{4+} ($3d^0$). Ti^{3+} ion in the ligand field demonstrates two absorption bands. The broad band due to the $^2T_{2g} \rightarrow E_g$ transition of the Ti^{3+} ion in octahedral (O_h) site symmetry is located in the spectral range from 480 to 625 nm depending on the ligand field strength and distortions of its symmetry [84,85]. The band due to the $E_g \rightarrow {}^2T_{2g}$ transition of Ti^{3+} ions in tetrahedral (T_d) site symmetry is located at ~1000 nm [85,86]. The O-Ti^{3+} oxygen to metal charge transfer (OMCT) band is in the UV spectral range at ~240 nm [87].

Ti^{4+} ions do not demonstrate d-d transitions due to empty 3d orbitals. They have the O-Ti^{4+} OMCT band, which is located in the UV spectral range at about 300 nm [88], as well as participate in homonuclear intervalence charge transfer (IVCT) Ti^{4+}/Ti^{3+} and heteronuclear IVCT $Fe^{2+} + Ti^{4+} \rightarrow Fe^{3+} + Ti^{3+}$ transitions that give rise to intense absorption bands in the visible spectral range. Traces of iron ions come to glass as impurities in raw materials. In different minerals, IVCT Ti^{4+}/Ti^{3+} transition gives rise to a band at ~480 nm [88] and at about 660 - 670 nm [89].

Figure 13(c) shows that the absorption edge, defined as the wavelength corresponding to an optical density equal to 1 (the absorption coefficient is 23 cm^{-1}), is located at 335 nm in the spectrum of the initial ZAS glass. It appears due to OMCT $O^{2-} \rightarrow Ti^{3+}$ and $O^{2-} \rightarrow Ti^{4+}$ transitions [90–92]. The spectrum also shows an unstructured absorption band in the region from 335 to 1000 nm, the tail of which extends to longer wavelengths, see Fig. 13(e). It is associated with the absorption of Ti^{3+} ions in O_h coordination (the transition $T_{2g} \rightarrow E_g$) and intervalence charge transfer (IVCT) $Ti^{3+} \rightarrow Ti^{4+}$ previously detected in silicate glasses [90–92]. Figure 13(g) demonstrates the broad unstructured absorption band in the 2700 - 3200 nm region, which appears due to the absorption of OH-groups in the initial glass [93,94].

After the heat-treatment of the initial ZAS glass at the nucleation stage, its absorption spectrum shows a slight shift of the absorption edge from 335 to 338 nm, and an increase in the intensity and broadening of the absorption band located in the visible and near-infrared spectral region (up to 1250 nm). A weak maximum at 2957 nm appears in the absorption band of OH-groups. The absorption edge in the spectrum of the ZAS GC obtained by the heat-treatment at 750 °C at the second stage does not change its position relative to the absorption edge in the spectrum

of the glass that underwent heat-treatment at the nucleation stage. The absorption edge in spectra of GCs obtained by two-stage heat-treatments gradually changes its position from 342 nm to 354 nm with increasing of the heat-treatment temperature from 800 to 950 °C. The pronounced shift of the absorption edge to 397 nm and then to 406 nm is observed in spectra of GCs obtained by heat-treatments at 1000 °C and 1050 °C at the second stage, respectively, Fig. 13(c). The absorption edge in ZAS GCs, as in glass, is formed by charge transfer bands $O^{2-} \rightarrow Ti^{3+}$ и $O^{2-} \rightarrow Ti^{4+}$ [10,11, 95-97]. In GCs obtained by heat-treatments at 1000 °C and 1050 °C scattering losses are superimposed with absorption edge.

In the spectra of GCs, the unstructured and broadband absorption in the visible and near-IR region intensifies with increasing the heat-treatment temperature at the second stage. This band is formed by short-wavelength bands with maxima at ~490 nm and ~590 nm and a longer-wavelength band whose maximum gradually shifts from ~760 nm to ~815 nm with increasing the heat-treatment temperature. The absorption coefficient of the latter band increases faster than the absorption coefficient of the band with a maximum at ~ 490 nm. The intensity of the absorption band with a maximum at ~590 nm sharply increases after heat-treatments at 900 °C and 950 °C, see Fig. 13(e).

It is generally accepted that titanium introduced to $ZnAl_2O_4$ is tetravalent and that titanium substituting Al^{3+} does not keep 3+ valence state [11,98]. We did not find any information about gahnite crystals doped with Ti^{3+} ions. That is why we had to refer to absorption of $MgAl_2O_4$ and Al_2O_3 crystals doped with Ti^{3+} ions in our interpretation of absorption spectra of ZAS GCs. Indeed, absorption spectra of ZAS GCs are very similar to the spectrum of Ti^{3+}: $MgAl_2O_4$ [55]. Based on this comparison [95-97,99,100], we may conclude that the broad band spanning from the visible to near IR spectral range is caused by absorption of Ti^{3+} ions in O_h coordination ($T_{2g} \rightarrow E_g$ transition) in gahnite crystals in positions of Al^{3+} and the charge transfer band $Ti^{4+} + Fe^{2+} \rightarrow Fe^{3+} + Ti^{3+}$ (iron is an inevitable admixture in raw materials) [53,95,96,98,101]. With increasing the heat-treatment temperature, the absorption band with a maximum at a wavelength of ~760 nm is broadened and extends into the near-IR region. After secondary heat-treatments at 1000 and 1050 °C, the intensity of the absorption band increases. There is also an increase in absorption in the whole spectral region up to the location of absorption bands of OH-groups. This raise of absorption correlates with the raise of gahnite crystallinity fraction with increasing the heat-treatment temperature, see Fig. 5(a).

Let us discuss absorption in the spectral range from 2650 to 3200 nm, which is due to OH-groups. After the two-stage heat-treatment with the temperature of 750 °C at the second stage, the shape of the absorption band drastically changes: the broad and unstructured band associated with the absorption of OH-groups in the glass splits into two bands. A broad band of lower intensity

spans from ~2670 to ~2870 nm. It has two maxima at ~2740 nm and ~2810 nm. The second band of much higher intensity locates in the spectral range from 2900 to 3100 nm. It has an asymmetric shape, which assumes an appearance of two maxima at ~2957 nm and ~3012 nm. In the spectra of GC samples obtained by two-stage heat-treatments with temperatures at the second stage in the range from 800 °C to 900 °C, an increase in the absorption intensity of both IR bands is observed. The higher wavelength band becomes narrower due to the disappearance of the band at ~3012 nm. In the spectra of these samples, the band due to the absorption of OH-groups in glass is difficult to notice. Intensity of the absorption band with a maximum at ~2957 nm in the spectra of GCs obtained by heat-treatment in the temperature range of 950 - 1050 ° C sharply decreases. The value of the absorption coefficient falls almost twice, from 6.8 cm^{-1} (900 °C) to 3.6 cm^{-1} (1050 °C). Absorption coefficient in the maximum of the band at ~ 2740 nm gradually increases from 1 cm^{-1} (750 °C) to 4.57 cm^{-1} (1050 °C), the band narrows, and its maximum shifts from ~2740 nm to ~2730 nm (950 °C) with increasing the heat-treatment temperature.

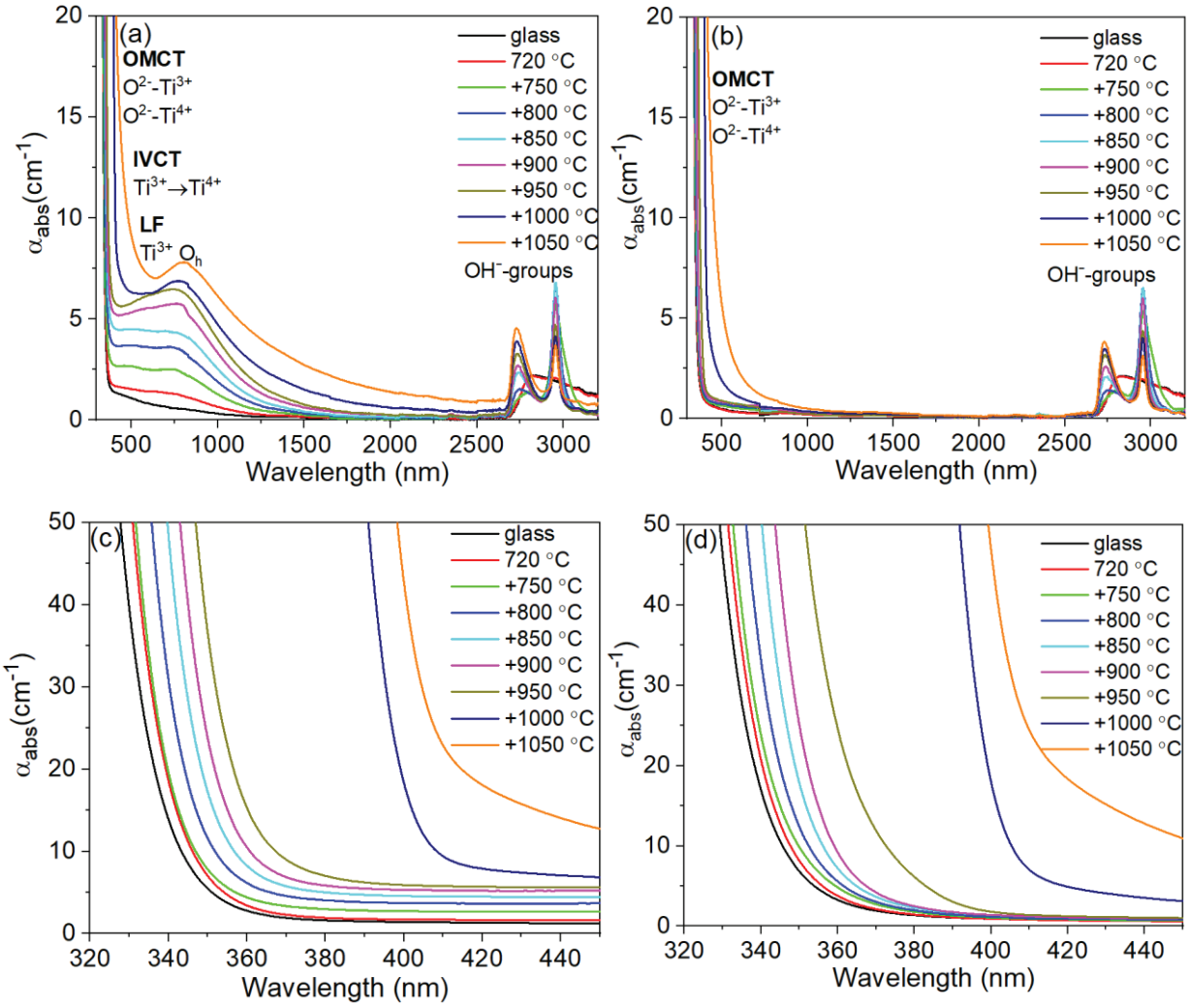

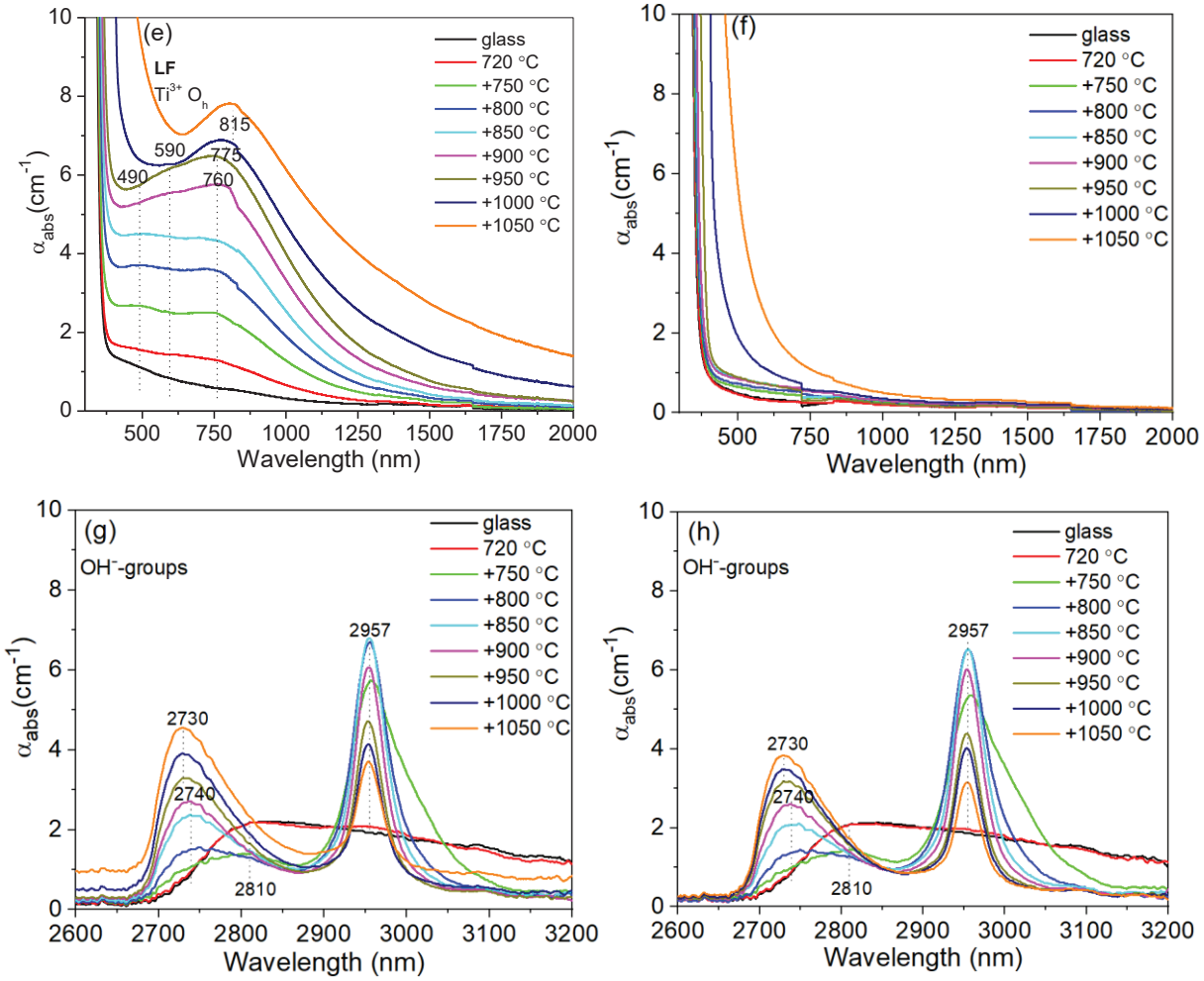

Fig. 13. Absorption spectra of the initial glass and transparent glass-ceramics in different spectral ranges: (a,b) the overview spectra; (c,d) a close look on the 320 – 450 nm range; (e,f) a close look on the 350 – 2000 nm range; (g,h) a close look on the OH^- -group absorption at 2600 – 3200 nm. Labels +750 … +1050 °C indicate the heat-treatment temperature at the second stage. The first stage of the heat-treatment is at 720 °C. The heat-treatment duration at each stage is 6 h. Numbers indicate the peak positions in nm.

In the spectrum of the initial ZAS_{ox} glass, the absorption edge is located at 337 nm, see Figure 13(b,d). It is due to the O^{2-} — Ti^{4+} charge transfer band [10,11,90-95]. Absence of absorption in the visible and near IR regions of the spectrum, Fig. 13(b), indicates the absence of a noticeable amount of Ti^{3+} ions in the ZAS_{ox} glass. The broad unstructured absorption band in the range from 2700 nm to 3200 nm, Fig. 13(b,h), is due to absorption of OH-groups in the initial glass [96,97]. The absorption edge shifts slightly from 337 to 339 nm after the nucleation heat-treatment of the ZAS_{ox} glass at 720 °C for 6 h. A slight structuring of the absorption band due to the presence of OH-groups is revealed by an appearance of a weak maximum at 2957 nm.

Figure 13(b) shows that after two-stage heat-treatments there is a gradual shift of the absorption edge to longer wavelengths and structuring of the band associated with OH-groups absorption. There is no absorption in the visible spectral range. Gahnite crystallization at these

heat-treatments probably causes accommodation of Ti^{4+} ions in its structure according to the scheme that two Al^{3+} ions are replaced with one Ti^{4+} and one Zn^{2+} ion [98].

The absorption edge in the spectrum of GC of the ZAS_{ox} composition, obtained by the heat-treatment at 750 °C at the second stage, practically does not change its position (there is a shift of 1 nm, from 339 nm to 340 nm) relative to the absorption edge in the spectrum of the glass that underwent the nucleation heat-treatment at 720 °C. The absorption edge in the spectra of GCs obtained by heat-treatments from 800 to 950 °C shifts to longer wavelengths from 344 nm to 361 nm with increasing the heat-treatment temperature. The absorption edge position in spectra of GCs obtained by the two-stage heat treatments with the temperatures of 1000 °C and 1050 °C at the second stage shifts to 398 nm and to 412 nm, respectively, suggesting an increase of scattering losses. This increase is caused by crystallization of gahnite crystals with a refractive index n = 1.79–1.80 [102,103], and rutile crystals with a higher refractive index $n_o = 2.5835$ and $n_e = 2.8650$ at 633 nm [104]. The analysis of the origin of light scattering in these GCs will be the subject of the future study within the framework of the approach developed by M. Shepilov *et al.* in Refs [105,106].

Intensification and structuring of OH-group absorption bands in the spectra of the ZASox GC obtained by heat-treatments from 750 to 1050 °C at the second stage occurs in the same way as in spectra of GCs of the ZAS composition.

4. Discussion

Previously we studied phase transformations in the glass of the ZAS_{ox} composition using the combination of XRD analysis, small-angle X-ray scattering and low-frequency Raman scattering [32] and revealed that the initial glass is inhomogeneous, which is proven by the present TEM results, see Fig.10(a,d). Upon heat-treatment, metastable amorphous phase separation develops in the glass by spinodal mechanism [32]. The glass demonstrates the bimodal structure, i.e. the appearance of inhomogeneous regions with large and small sizes and different compositions regularly distributed in the residual glass. The rate of formation of large zinc aluminotitanate regions of inhomogeneity is much higher than that of the smaller zinc aluminate regions, and zinc aluminotitanate phase predominantly precipitates upon cooling, quenching and annealing of the initial glass. The zinc aluminate phase is mainly formed during subsequent heat treatments, while the formation of zinc aluminotitanate phase continues during these heat-treatments. Both types of inhomogeneous regions also contain some SiO_2 in their compositions. In the course of phase separation, the residual glass becomes silica-enriched and thus more viscous. Gahnite crystallizes from the zinc aluminate amorphous phase during heat-treatments at 750 °C

and above, while the zinc aluminotitanate amorphous phase decomposes at 1000 °C with crystallization of rutile and additional crystallization of gahnite [32].

In the present study, we compared the structure and some physical properties of GCs prepared from the same glass melted in oxidizing and normal conditions. The presence of some portion of Ti^{3+} ions in the ZAS glass melted under normal conditions and their absence in the ZAS_{ox} glass melted under oxidizing conditions is proven by the comparison of their absorption spectra.

The increase of the absorption due to Ti^{3+} ions after the heat-treatment of the ZAS glass at the nucleation stage suggests that Ti^{3+} ions enter the amorphous phase separated regions. A further increase of absorption due to Ti^{3+} ions after the heat-treatment at 750 °C, when gahnite crystals with structure corresponding to a normal spinel appear in ZAS GC, proves that Ti^{3+} ions enter the zinc aluminotitanate amorphous phase. Simultaneous growth of absorption due to Ti^{3+} ions in O_h positions and of the gahnite crystallinity fraction in the ZAS GC at increasing the temperature of heat-treatment, suggests that Ti^{3+} ions do enter into zinc aluminate amorphous regions and, at their crystallization, into gahnite crystals substituting for octahedrally coordinated Al^{3+} ions by the isovalent isomorphism scheme; the broadband absorption is due to the $^2T_{2g} \rightarrow E_g$ transition of Ti^{3+} ions in the octahedral positions of gahnite crystals.

Thus, we obtained Ti^{3+}-doped gahnite nanocrystals for the first time, to the best of our knowledge.

In the structure of normal gahnite, tetrahedral positions are occupied by Zn^{2+} ions and octahedral positions by Al^{3+} ions. The incorporation of Ti^{4+} ions into the gahnite structure occurs as a result of heterovalent isomorphism according to the scheme $Zn^{2+} + Ti^{4+} \leftrightarrow 2Al^{3+}$. According to [11,98], charge balance in Ti^{4+}-doped gahnite samples and stabilization of their crystal structure is achieved by substituting a portion of Al^{3+} ions on octahedral sites with excess Zn^{2+} ions. We suggest that in ZAS_{ox} GCs titanium enters into gahnite structure as Ti^{4+} ion, substituting for octahedrally coordinated Al^{3+} ions, which is confirmed by appearance of additional gahnite bands in Raman spectra of ZAS_{ox} GCs [72,73]. The unit cell parameter of gahnite in this case increases.

The dependences of the gahnite unit cell parameter *a* on the heat-treatment temperature for the samples 9ZAS and $9ZAS_{ox}$ near coincide, see Fig. 6. Crystallization of gahnite begins at the heat-treatment temperature of 750 °C, and the unit cell parameter of gahnite crystals formed at this temperature is near 8.087 Å, which corresponds to the literature data for normal spinel. An increase of the heat-treatment temperature leads to growth of the gahnite crystallinity fraction. The parameter *a* of the gahnite unit cell increases and takes the value ~8.110 Å. The increase in the parameter *a* may be due to entering the titanium ions into the gahnite structure as an impurity. The appearance of the band at ~732 cm^{-1} in the Raman spectra of ZAS and ZAS_{ox} GCs confirms this

assumption. It can be assumed that in both GCs Ti ions enter the structure of gahnite mainly in the 4+ oxidation state, which is in agreement with the results of Refs [72,98]. It means that the impact of Ti^{3+} ions on the gahnite parameter *a* is small probably due to the small fraction of Ti^{3+} ions in the initial ZAS glass.

The parameter *a* of the gahnite unit cell could be considered unchanged in the whole temperature range of heat-treatments from 850 °C to 1350 °C for both GCs, if it were not for the synchronous decrease of the parameter in GCs prepared by heat-treatments in the range from 1000 °C to 1100 °C. The decreased value of *a* = 8.104 Å in the ZAS samples is observed at heat-treatment temperatures of 1050 °C and 1100 °C, and in ZAS_{ox} samples *a* = 8.105 Å at 1000 °C and 1050 °C. It is noteworthy that the beginning of rutile crystallization is observed at 1000 °C according to XRD data. Crystallization of rutile in the zinc aluminotitanate amorphous phase provokes the crystallization of gahnite. Consequently, the amorphous zinc aluminotitanate phase is an additional source of gahnite formation. It is possible that the gahnite crystallizing in the aluminotitanate phase has a unit cell parameter much lower than that of gahnite crystallized from the zinc aluminate amorphous phase. There may be several reasons for this. One of them may be the different ratio of ZnO and Al_2O_3 components in these amorphous phases. It is known that the unit cell parameter of gahnite decreases if the content of ZnO decreases by increasing the content of Al_2O_3. Thus, the parameter of gahnite with the composition of $(Zn_{0.3}Al_{0.7})Al_{1.7}O_4$ (ISCD card #77-0732) is 8.000 Å. Another reason may be the absence or a reduced content of titanium ions in gahnite crystallizing from the zinc aluminotitanate phase simultaneously with rutile. The presence of some amount of gahnite with a low unit cell parameter may reduce the total value of the gahnite parameter. The decrease of the gahnite unit cell parameter at the heat-treatment temperature of 1000 °C for the ZAS_{ox} GC and of 1050 °C for the ZAS GC allows us to confirm the conclusion that the decomposition of the zinc aluminotitanate phase and the crystallization of rutile in ZAS_{ox} GCs occurs at a lower temperature than in ZAS GCs. This is another difference in the temperature of phase transformations related to synthesis conditions.

Variation of the redox conditions of glass melting applied in this study does not influence significantly the sequence and character of phase transformations in the ZAS glasses. However, in the initial glass obtained under oxidizing conditions, liquid phase separation develops faster than in the sample obtained under normal conditions. Variation of the redox conditions of glass melting affects also the temperature of rutile and cristobalite crystallization. In the ZAS_{ox} GCs, crystallization of rutile and of the residual glass begins at a lower heat-treatment temperature as compared with that for the ZAS glass, which can be explained by the role of titanium ions. It was demonstrated that Ti^{4+} ions can induce the formation of cristobalite [107]. An analysis of changes in the unit cell parameters of rutile in GCs obtained from glasses melted under different redox

conditions showed that the conditions of glass synthesis affect the structure of rutile formed after heat treatment at temperatures from 1050 °C to 1200°C. The unit cell of rutile in GCs obtained from glasses synthesized under oxidizing conditions has a more elongated shape than the unit cell of rutile in GCs obtained from glasses melted under reducing conditions. Such a change in the parameters is possibly due to the fact that Ti^{3+} ions are present in rutile as an impurity. The size of rutile crystals formed in GCs after heat treatment in the temperature range from 1050 °C to 1200 °C is not affected by the synthesis conditions.

The analysis of the absorption spectra leads to the conclusion that the redox conditions of glass melting influence the composition of the gahnite crystals. Comparison of the absorption spectra of the initial glass, the glass that underwent the heat-treatment at the nucleation stage, and the GCs of the ZAS composition with those of the ZAS_{ox} composition indicates that the spectra differ in the range from 335 to 1700 nm. This difference is due to the different nature of the absorbing centers in the samples. The spectra of samples obtained under oxidizing conditions are dominated by Ti^{4+} ions. In the spectra of samples obtained under normal conditions, the broadband absorption is due to the $^2T_{2g} \rightarrow E_g$ transition of Ti^{3+} ions in the octahedral positions in gahnite crystals.

Let us discuss the behavior of the OH- band in absorption spectra of the ZAS and ZAS_{ox} glasses. It is known [108] that the nominally anhydrous materials can incorporate significant amounts of dissolved 'water' in the form of structurally incorporated hydrogen (H^+), which is typically bound to relatively underbonded oxygens, forming spectroscopically active hydroxyl (OH^-) groups. These groups are often associated with other defects such as cation vacancies. Most of the stretching vibrations of trace OH- groups in minerals are observed in the high-energy region between 3700 and 3200 cm^{-1} [109]. There exists a correlation between O-O distances of protonated polyhedral edges in minerals and O-H stretching frequencies [110].

The position of the broad unstructured band connected with OH- groups in glasses and GCs under study falls in this spectral region. The band due to the absorption of OH- groups in the initial ZAS and ZAS_{ox} glasses is broad and asymmetric with a maximum at a wavelength of ~2800 nm (~3570 cm^{-1}), with a tail to lower energies indicating a broad distribution of H bond lengths [111].

As we mentioned above, after the two-stage heat-treatment with the temperature of 750 °C at the second stage, the shape of the absorption band drastically changes: the broad and unstructured band associated with the absorption of OH-groups in the glass splits into two bands. Different dependences of intensities of absorption bands of OH- groups on the heat-treatment temperature - the increase in the intensity of the absorption band at 2730 nm (3663 cm^{-1}), and first the growth and then the decrease in the intensity of the band at 2957 nm (3382 cm^{-1}), apparently,

indicates that these bands are also due to the absorption of OH- groups in different environments. We believe that OH- groups are located in different phases of multiphase GCs.

A weak maximum at 2957 nm appears in the spectrum after the heat-treatment at the nucleation stage, when amorphous phase separation develops. Intensity of this maximum grows with the increase of the heat-treatment temperature up to 850 °C and decreases with a further increase of the heat-treatment temperature in the range from 900 to 1050 °C. According to Raman spectroscopy data, the intensity of the band connected with the zinc aluminotitanate amorphous phase behaves in a similar way, see Fig. 9. During heat-treatments at temperatures from ~900 °C, partially ordered rutile-like regions are formed, and then rutile and gahnite crystallization begins in the amorphous zinc aluminotitanate regions (the latter is confirmed by XRD data). It can be assumed that the solubility of OH-groups in the zinc aluminotitanate regions decreases upon rutile and gahnite crystallization, while the rate of their diffusion from these regions increases. This should lead to a decrease in the intensity of the absorption band of OH-groups in this phase. Thus, it can be suggested that the absorption band of OH groups with a maximum of ~2957 nm is associated with OH- groups in amorphous zinc aluminotitanate regions, and the decrease in the intensity of this band is presumably associated with the onset of structural transformations in these regions. It should be noted that rutile from natural occurrences is characterized by one or two absorption bands in the 3300 cm^{-1} region located between 3320 and 3280 cm^{-1} (3012 - 3049 nm) [112]. It is difficult to find such bands in absorption spectra of our GCs.

According to Refs [108,113] synthetic, non-stoichiometric, Al-rich spinel can incorporate significant quantities of hydroxyl as opposed to stoichiometric spinel. We assume that the band with a maximum of ~2730 nm (~3663 cm^{-1}) is due to the absorption of OH- groups in gahnite nanocrystals in GCs, since this peak appears simultaneously with gahnite crystallization upon heat-treatment at 750 °C and its intensity increases with an increase in the spinel fraction in GCs, see Fig. 14. It should be noted that the band at the same position appears in the spectrum of GC of the magnesium aluminosilicate system simultaneously with crystallization of magnesium aluminate spinel [83]. The position of this absorption band is different from the position of the band at around 2890 nm (3460 cm^{-1}) presented in Ref. [114] and assigned to the OH- stretching vibrations in synthetic gahnite crystals and from the position of the broad absorption band in the spectrum of naturally occurring gahnite crystals (ZnA_2O_4) at ~2940 nm (3400 cm^{-1}) [115]. However, the position of this band is close to that of the γ-Mg_2SiO_4 phase with spinel structure, for which the IR spectrum shows very broad absorption bands centered at 2743 nm (3645 cm^{-1}) and 2989 nm (3345 cm^{-1}) with a shoulder at 3226 nm (3120 cm^{-1}) [116]. It allows us to suggest that the hydrogen ions are associated with oxygen ions in the gahnite crystals near the grain boundaries between the gahnite crystals and the residual glass. OH- groups in silica glass are characterized by a single IR

band at ~2729 nm (3665 cm^{-1}) with inflections at ~2774 nm (3605 cm^{-1}) and at ~2710 nm (3690 cm^{-1}) [117], which is difficult to notice on the background of the band associated with OH- groups in gahnite.

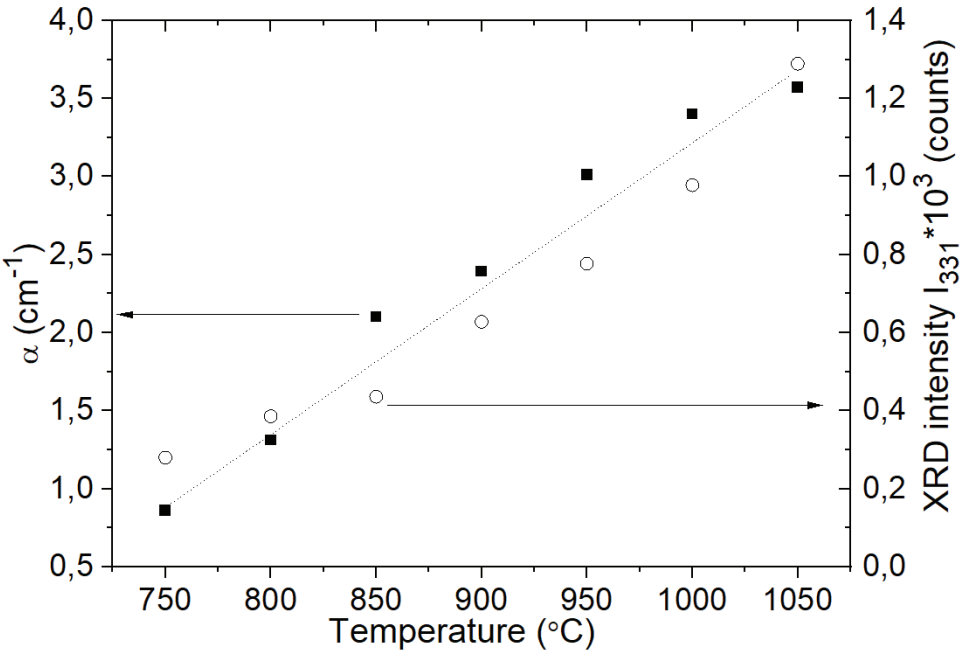

Fig. 14. Variation of the absorption coefficient at λ = 2730 nm and variationof the gahnite XRD peak intensity I_{331} with the heat-treatment temperature.

Conclusions

The influence of redox conditions of glass melting on the sequence of phase transformations, structure, spectral and physical properties of titanium-containing glass-ceramics based on nanosized gahnite crystals has been studied for the first time, to the best of our knowledge.

The model glass of the zinc aluminosilicate system nucleated by titania was melted with and without addition of As_2O_3. The glasses were subjected to heat-treatments in the temperature range from 720 to 1350 °C to obtain gahnite-based glass-ceramics. The structure and spectroscopic properties of these materials were studied by the DSC, XRD analysis, TEM, Raman and absorption spectroscopy. Their density and thermal expansion coefficients were determined.

Initial glasses are X-ray amorphous while inhomogeneous. The glass melted in normal conditions as opposed to glass melted in oxidizing conditions contains Ti^{3+} ions. Upon heat-treatment at the nucleation stage, metastable amorphous phase separation develops, and titanium ions in different oxidation states are distributed between inhomogeneous regions different in composition and sizes, and the residual glass phase.

The zinc aluminate amorphous phase, which also contains traces of titanium ions, crystallizes with formation of Ti-doped gahnite nanosized crystals with a cubic spinel structure during heat-treatments in the range from 750 to 1350 °C. The zinc aluminotitanate amorphous phase decomposes with crystallization of rutile and additional crystallization of gahnite at temperatures of 1000 °C and above.

Gahnite unit cell parameters of ZAS and ZAS_{ox} GCs change with the heat-treatment temperature in a similar way due to incorporation of titanium ions mainly in Ti^{4+} oxidation state. The impact of Ti^{3+} ions on the gahnite unit cell parameter is not noticeable due to a small fraction of Ti^{3+} ions in ZAS GCs.

Variation of the redox conditions of glass melting affects the distribution of Ti^{3+} and Ti^{4+} ions between the amorphous and crystalline phases, kinetics of liquid phase separation and crystallization of rutile and the residual glass phase.

Variation of the redox conditions of glass melting does not affect the kinetics of crystallization of nanosized gahnite crystals and the structure of thus obtained glass-ceramics. This finding is very promising for the development of glass-ceramics doped with the functional ions in the lower oxidation state.

Transparent glass-ceramics based on titanium-doped gahnite were obtained by two-stage heat-treatments in the temperature range from 750 °C to 1050 °C. In ZAS GCs obtained from glasses melted under normal conditions, broadband absorption is observed in the visible and near-IR due to absorption of Ti^{3+} ions located in O_h positions in $ZnAl_2O_4$ crystals.

Changing the redox conditions of glass melting makes it possible to control the content of titanium ions in various oxidation states in $ZnAl_2O_4$ nanocrystals and the spectral properties of glass-ceramics, which is important for the development of promising materials for laser technology including the rare-earth-free phosphors.

Acknowledgement

This work was partly supported by the Russian Science Foundation (Grant 23-23-00446).

References

1. N.J. van der Laag, M.D. Snel, P.C.M.M. Magusin, G. de With, Structural, elastic, thermophysical and dielectric properties of zinc aluminate ($ZnAl_2O_4$), J. Eur. Ceram., 24(8) (2004) 2417–2424. https://doi.org/10.1016/j.jeurceramsoc.2003.06.001.

2. S. Mandal, J.G. Hemrick, M.K. Mahapatra, Zinc aluminate ($ZnAl_2O_4$) refractory aggregates: Dilatometric sintering studies and thermal expansion coefficient, J. Eur. Ceram., 42(13) (2022) 6244–6254. https://doi.org/10.1016/j.jeurceramsoc.2022.06.058.

3. D.L. Ge, Y.J. Fan, C.L. Qi, Z.X. Sun, Facile synthesis of highly thermostable mesoporous $ZnAl_2O_4$ with adjustable pore size, J. Mater. Chem. A 1 (2013) 1651–1658. https://doi.org/10.1039/c2ta00903j.

4. U. Hålenius, G.B. Andreozzi, H. Skogby, Structural relaxation around Cr^{3+} and the red-green color change in the spinel (sensu stricto)-magnesiochromite ($MgAl_2O_4$-$MgCr_2O_4$) and gahnite-zincochromite ($ZnAl_2O_4$-$ZnCr_2O_4$) solid-solution series, Am. Mineral. 95(4) (2010) 456–462. https://doi.org/10.2138/am.2010.3388.

5. V.D'Ippolito, G.B.Andreozzi, F.Bosi, U.Halenius, L.Mantovani, D.Bersani, R.A.Fregola, Crystallographic and spectroscopic characterization of a natural Zn-rich spinel approaching the endmember gahnite ($ZnAl_2O_4$) composition, Mineral. Mag. 77(7) (2013) 2941–2953, https://doi.org/10.1180/minmag.2013.077.7.05.

6. R.A. Fregola, H. Skogby, F. Bosi, V. D'Ippolito, G.B. Andreozzi, U. Hålenius, Optical absorption spectroscopy study of the causes for color variations in natural Fe-bearing gahnite: Insights from iron valency and site distribution data, Am. Mineral. 99 (2014) 2187–2195. https://doi.org/10.2138/am-2014-4962.

7. H. Saalfeld, Strukturdaten von gahnit, $ZnAl_2O_4$, Z. fur Krist. - Cryst. Mater. 120(1-6) (1964) 476–478. https://doi.org/10.1524/zkri.1964.120.16.476.

8. G. Lorenzi, G. Baldi, F. Di Benedetto, V. Faso, P. Lattanzi, M. Romanelli, Spectroscopic study of a Ni-bearing gahnite pigment, J. Eur. Ceram. Soc. 26(3) (2006) 317–321. https://doi.org/10.1016/j.jeurceramsoc.2004.10.027.

9. J. Popović, E. Tkalčec, B. Gržeta, S. Kurajica, B. Rakvin, Inverse spinel structure of Co-doped gahnite, Am. Mineral. 94 (2009) https://doi.org/771–776. 10.2138/am.2009.3173.

10. M.T. Tsai, Y.S. Chang, Y.H. Chou, K.M. Tsai, Photoluminescence of titanium-doped zinc spinel blue-emitting nanophosphors, J. Solid State Chem. 214 (2014) 86–90. https://doi.org/10.1016/j.jssc.2013.10.019.

11. P.J. Dereń, D. Stefańska, M. Ptak, M. Mączka, W. Walerczyk, G. Banach Origin of violet-blue emission in Ti-doped gahnite, J. Am. Ceram. Soc. 97(6) (2014) 1883–1889, https://doi.org/10.1111/jace.12858.

12. J. Popović, B. Gržeta, B. Rakvin, E. Tkalčec, M. Vrankić, S. Kurajica, Partial inverse spinel structure of manganese-doped gahnite: XRD and EPR spectroscopy studies, J. Alloys Compd. 509(34) (2011) (8487–8492). https://doi.org/10.1016/j.jallcom.2011.06.006.

13. N.M. Khaidukov, M.N. Brekhovskikh, N.Yu. Kirikova, V.A. Kondratyuk, V.N. Makhov, Luminescence of $MgAl_2O_4$ and $ZnAl_2O_4$ spinel ceramics containing some 3d ions, Ceram. Int. 46(13) (2020) 21351–21359. https://doi.org/10.1016/j.ceramint.2020.05.231.

14. K. Kamada, Y. Shoji, A. Yamaji, S. Kurosawa, Yuui Yokota, Y. Ohashi, Kyoung Jin Kim, M. Ivanov, V.V. Kochurikhin, A. Yoshikawa, Melt growth of zinc aluminate spinel single crystal by the micro-pulling down method under atmospheric pressure, J. Cryst. Growth 492 (2018) 67–70. https://doi.org/10.1016/j.jcrysgro.2018.03.009.

15. H.St.C. O'Neill, W.A. Dollase, Crystal structures and cation distributions in simple spinels from powder XRD structural refinements: $MgCr_2O_4$, $ZnCr_2O_4$, Fe_3O_4 and the temperature dependence of the cation distribution in $ZnAl_2O_4$, Phys. Chem. Miner. 20 (1994) 541–555. https://doi.org/10.1007/BF00211850.

16. K. Kumar, K. Ramamoorthy, R. Chandramohan, K. Sankaranarayanan, Bulk crystal growth of zinc aluminate spinel at room temperature, Adv. Appl. Ceram. 104 (2005) 291–293. https://doi.org/10.1179/aac.2005.104.6.291.

17. K. Kumar, K. Ramamoorthy, R. Chandramohan, K. Sankaranarayanan, A novel growth method for $ZnAl_2O_4$ single crystals, Cryst. Res. Technol. 41 (2006) 217–220. https://doi.org/10.1002/crat.200510562.

18. A. Goldstein, Y. Yeshurun, M. Vulfson, H. Kravits, Fabrication of transparent polycrystalline $ZnAl_2O_4$ – a new optical bulk ceramic, J. Am. Ceram. Soc. 95 (2012) 879–882. https://doi.org/10.1111/j.1551-2916.2011.05063.x.

19. B.N. Kim, K. Hiraga, A. Jeong, C. Hu, T.S. Suzuki, J.D. Yun, Y. Sakka, Transparent $ZnAl_2O_4$ ceramics fabricated by spark plasma sintering, J. Ceram. Soc. Jpn. 122 (2014) 784–787. https://doi.org/10.2109/jcersj2.122.784.

20. Y. Xu, P. Fu, B.H. Zhang, J. Gao, L. Zhang, X.H. Wang, Optical properties of transparent $ZnAl_2O_4$ ceramics: A new transparent material prepared by spark plasma sintering, Mater. Lett. 123 (2014) 142–144. https://doi.org/10.1016/j.matlet.2014.03.013.

21. A.V. Belyaev, I.I. Evdokimov, V.V. Drobotenko, A.A. Sorokin, A new approach to producing transparent $ZnAl_2O_4$ ceramics, J. Eur. Ceram. Soc. 37 (2017) 2747–2751. https://doi.org/10.1016/j.jeurceramsoc.2017.02.041.

22. P. Fu, Z.Y. Wang, Z.D. Lin, Y.Q. Liu, V.A.L. Roy, The microwave dielectric properties of transparent $ZnAl_2O_4$ ceramics fabricated by spark plasma sintering, J. Mater. Sci. 28 (2017) 9589–9595. https://doi.org/10.1007/s10854-017-6707-y.

23. V. Fedorov, B.K. Coyne, K. Karki, S. Balabanov, A. Belyaev, V. Smolski, S. Subedi, S. Mirov, Spectroscopic characterization of Fe:$ZnAl_2O_4$, Fe:$MgAl_2O_4$ and Fe:InP crystals for mid-IR laser applications, Proc. SPIE 11259, Solid State Lasers XXIX: Technology and Devices, 112591A (21 February 2020). https://doi.org/10.1117/12.2546501.

24. P. Loiko, A. Belyaev, O. Dymshits, I. Evdokimov, V. Vitkin, K. Volkova, M. Tsenter, A. Volokitina, M. Baranov, E. Vilejshikova, A. Baranov, A. Zhilin, Synthesis, characterization and

absorption saturation of Co:$ZnAl_2O_4$ (gahnite) transparent ceramic and glass-ceramics: A comparative study, J. Alloys Compd. 725 (2017) 998–1005. https://doi.org/10.1016/j.jallcom.2017.07.239.

25. S.F. Wang, G.Z. Sun, L.M. Fang, L. Lei, X. Xiang, X.T. Zu, A comparative study of $ZnAl_2O_4$ nanoparticles synthesized from different aluminum salts for use as fluorescence materials. Sci. Rep. 5 (2015) 12849(1–12). https://doi.org/10.1038/srep12849.

26. G.H. Beall, D.A. Duke, Transparent glass-ceramics, J. Mater. Sci. 4 (1969) 340–352. https://doi.org/10.1007/BF00550404.

27. A.J. Stryjak, P.W. McMillan, Microstructure and properties of transparent glass-ceramics, J. Mater. Sci. 13 (1978) 1794–1804. https://doi.org/10.1007/BF00548743.

28. Z. Strnad, Glass-Ceramic Materials, Elsevier, Amsterdam, The Netherland (1986), 101–105.

29. L.R. Pinckney, Transparent glass-ceramics containing gahnite. U.S. Patent No. 4 687 750; 1987.

30. L.R. Pinckney, Transparent, high strain point spinel glass-ceramics. J. Non-Cryst. Solids 255 (1999) 171–177. https://doi.org/10.1016/S0022-3093(99)00368-3.

31. G.H. Beall, L.R. Pinckney, Nanophase glass-ceramics, J. Am. Ceram. Soc. 82 (1999) 5–16. https://doi.org/10.1111/j.1151-2916.1999.tb01716.x.

32. V.V. Golubkov, O.S. Dymshits, V.I. Petrov, A.V. Shashkin, M.Ya. Tsenter, A.A. Zhilin, U. Kang, Small-angle X-ray scattering and low-frequency Raman scattering study of liquid phase separation and crystallization in titania-containing glasses of the ZnO-Al_2O_3-SiO_2 system. J. Non-Cryst. Solids 351 (2005) 711–721. https://doi.org/10.1016/j.jnoncrysol.2005.01.071.

33. E. Tkalčec, S. Kurajica, H. Ivanković, Crystallization behavior and microstructure of powdered and bulk ZnO–Al_2O_3–SiO_2 glass-ceramics, J. Non-Cryst. Solids 351 (2005) 149–157. https://doi.org/10.1016/j.jnoncrysol.2004.09.024.

34. A.R. Molla, A.M. Rodrigues, S.P. Singh, R.F. Lancelotti, E.D. Zanotto, A.C.M. Rodrigues, M.R. Dousti, A.S.S. de Camargo, C.J. Magon, I.A.A. Silva, Crystallization, mechanical, and optical properties of transparent, nanocrystalline gahnite glass-ceramics, J. Am. Ceram. Soc. 100 (2017) 1963–1975. https://doi.org/10.1111/jace.14753.

35. A.L. Mitchel, D.E. Perea, M.G. Wirth, J.V. Ryan, R.E. Youngman, A. Rezikyan, A.J. Fahey, D.K. Schreiber, Nanoscale microstructure and chemistry of transparent gahnite glass-ceramics revealed by atom probe tomography, Scr. Mater. 203 (2021) 114110(1–6). https://doi.org/10.1016/j.scriptamat.2021.114110.

36. S. Kurajica, J. Šipušić, M. Zupancic, I. Brautović, M. Albrecht, ZnO-Al_2O_3-SiO_2 glass ceramics: Influence of composition on crystal phases, crystallite size and appearance, J. Non-Cryst. Solids 553 (2021) 120481(1–8). https://doi.org/10.1016/j.jnoncrysol.2020.120481.

37. Y. Guo, Y. Lu, C. Liu, J. Wang, J. Han, J. Ruan, Effect of $ZnAl_2O_4$ crystallization on ion-exchange properties in aluminosilicate glass, Alloys Compd. 851 (2021) 156891(1–8). https://doi.org/10.1016/j.jallcom.2020.156891.

38. R.F. Cooley, J.S. Reed, Equilibrium cation distribution in $NiAl_2O_4$, $CuAl_2O_4$, and $ZnAl_2O_4$ spinels, J. Am. Ceram. Soc. 55 (1972) 395–398. https://doi.org/10.1111/j.1151-2916.1972.tb11320.x.

39. S. Mathur, M. Veith, M. Haas, A. Shen, N. Lecerf, V. Huch, S. Hufner, R. Haberkorn, H.P. Beck, M. Jilavi, Single-source sol-gel synthesis of nanocrystalline $ZnAl_2O_4$: Structural and optical properties. J. Am. Ceram. Soc. 84 (2001) 1921–1928. https://doi.org/10.1111/j.1151-2916.2001.tb00938.x.

40. G. Confalonieri, N. Rotiroti, A. Bernasconi, M.Dapiaggi, Structural study of nano-sized gahnite ($ZnAl_2O_4$): From the average to the local scale. Nanomaterials 10 (2020) 824(1–11). https://doi.org/ 10.3390/nano10050824.

41. S. Sommer, E.D. Bøjesen, N. Lock, H. Kasai, J. Skibsted, E. Nishibori, Bo B. Iversen, Probing the validity of the spinel inversion model: a combined SPXRD, PDF, EXAFS and NMR study of $ZnAl_2O_4$, Dalton Trans. 49 (2020) 13449–13461. https://doi.org/10.1039/D0DT02795B.

42. J.C. Waerenborgh, M.O. Figueiredo, J.M.P. Cabral, L.C.J. Pereira, Temperature and composition dependence of the cation distribution in synthetic $ZnFe_yAl_{2-y}O_4$ ($0 \leq y \leq 1$) spinels. J. Solid State Chem. 111(2) (1994) 300–309. https://doi.org/10.1006/jssc.1994.1231.

43. E.N. Bunting, Phase equilibria in the system SiO_2-ZnO-Al_2O_3, J. Res. Natl. Inst. Stand. Technol. 8 (1932) 279–287. https://dx.doi.org/10.6028/jres.008.020.

44. L. Jiazhi, S. Ying, H. Guanging, An investigation of relationship between phase separation and crystallization of ZnO-Al_2O_3-SiO_2 glasses, J. Phys. Colloques 43 (1982) 231–234. https://doi.org/10.1051/jphyscol:1982941.

45. R. Hansson, B. Zhao, P.C. Hayes, E. Jak, A reinvestigation of phase equilibria in the system Al_2O_3-SiO_2-ZnO, Metall. Mater. Trans. B 36 (2005) 187–193. https://doi.org/10.1007/s11663-005-0019-y.

46. L. Cormier, L. Delbes, B. Baptiste, V. Montouillout, Vitrification, crystallization behavior and structure of zinc aluminosilicate glasses, J. Non. Cryst. Solids 555 (2021) 120609(1–11). https://doi.org/10.1016/j.jnoncrysol.2020.120609.

47. R.M. Da Silva, A. Zeidler, H. Mohammadi, L.V.D. Gammond, E.G. Lange, R.E. Youngman, B.G. Aitken, A.C. Hannon, C.J. Benmore, G.B.M. Vaughan, P.S. Salmon, Mapping the structural trends in zinc aluminosilicate glasses, J. Chem. Phys. 159 (2023) 064501(1–16). https://doi.org/10.1063/5.0157790.

48. W. Wisniewski, K. Thieme, C. Rüssel, Fresnoite glass-ceramics – A review, Prog. Mater. Sci., 98 (2018) 68–107. https://doi.org/10.1016/j.pmatsci.2018.05.002.

49. W. Vogel, Glass Chemistry, Springer Berlin, Heidelberg, 1994, 464 p https://doi.org/10.1007/978-3-642-78723-2.

50. W. Höland, P. Wange, K. Naumann, J. Vogel, G. Carl, C. Jana, W. Götz, Control of phase formation processes in glass-ceramics for medicine and technology, J. Non-Cryst. Solids 129 (1991) 152–162. https://doi.org/10.1016/0022-3093(91)90091-J.

51. R. Keding, C. Rüssel, Electrochemical nucleation for the preparation of oriented glass ceramics, J. Non-Cryst. Solids, 219 (1997) 136–141. https://doi.org/10.1016/S0022-3093(97)00267-6.

52. T. Höche, H.-J. Kleebe, R. Brydson Can fresnoite ($Ba_2TiSi_2O_8$) incorporate Ti^{3+} when crystallizing from highly reduced melts? Philos. Mag. A, 81(4) (2001) 825–839. https://doi.org/:10.1080/01418610151133258.

53. L.E. Bausá, F. Jaque, J. Garcia Sole, A. Duran, Photoluminescence of Ti^{3+} in P_2O_5-Na_2O-Al_2O_3 glass, J. Mater. Sci. 23 (1988) 1921–1922. https://doi.org/10.1007/BF01115751.

54. K. Eremeev, O. Dymshits, I. Alekseeva, A. Khubetsov, S. Zapalova, M. Tsenter, L. Basyrova, P. Loiko, A. Zhilin, V. Popkov, Spectral properties of novel transparent glass-ceramics based on Fe^{2+}:$ZnAl_2O_4$ nanocrystals, J. Phys. Conf. Ser. 1697 (2020) 012125(1–6). https://doi.org/10.1088/1742-6596/1697/1/012125.

55. L.E. Bausá, I. Vergara, J. García-Solé, W. Strek, P.J. Deren, Laser-excited luminescence in Ti-doped $MgAl_2O_4$ spinel, J. Appl. Phys. 68 (1990) 736–740. http://dx.doi.org/10.1063/1.346807.

56. I. Alekseeva, A. Baranov, O. Dymshits, V. Ermakov, V. Golubkov, M. Tsenter, A. Zhilin, Influence of CoO addition on phase separation and crystallization of glasses of the ZnO–Al_2O_3–SiO_2–TiO_2 system, J. Non-Cryst. Solids 357 (2011) 3928–3939. https://doi.org/10.1016/j.jnoncrysol.2011.08.011.

57. T. Hayashi, W.G. Dorfeld, Electrochemical study of As^{3+}/As^{5+} equilibrium in a barium borosilicate glass melt, J. Non-Cryst. Solids, 177 (1994) 331–339, https://doi.org/10.1016/0022-3093(94)90547-9.

58. P. Scherrer, Bestimmung der Größe und der inneren Struktur von Kolloidteilchen mittels Röntgenstrahlen, J. Abh. Akad. Wiss. Gött., Math.-Phys. Kl. 2 (1918) 98–100. http://eudml.org/doc/59018.

59. H. Lipson, H. Steeple, Interpretation of X-ray powder patterns, ed. McMillan. London, N.-Y., Martins Press, 1970, 383 p.

60. D.E. Damby, E.W. Llewellin, C.J. Horwell, B.J. Williamson, J. Najorka, G. Cressey, M. Carpenter, The α–β phase transition in volcanic cristobalite, J. Appl. Cryst. 47 (2014) 1205–1215. https://doi.org/10.1107/S160057671401070X.

61. M.A. Carpenter, E.K.H. Salje, A. Graeme-Barber, Spontaneous strain as a determinant of thermodynamic properties for phase transitions in minerals, Eur. J. Mineral. 10 (1998) 621–691. https://doi.org/10.1127/ejm/10/4/0621.

62. P. McMillan, B. Piriou, A. Navrotsky, A Raman spectroscopic study of glasses along the joins silica-calcium aluminate, silica-sodium aluminate, and silica-potassium aluminate, Geochim. Cosmochim. Acta 46(11) (1982) 2021–2037. https://doi.org/10.1016/0016-7037(82)90182-X.

63. S. Sakka, F. Miyaji, K. Fukumi, Structure of binary K_2O-TiO_2 and Cs_2O-TiO_2 glasses, J. Non-Cryst. Solids 112 (1989) 64–68. https://doi.org/10.1016/0022-3093(89)90494-8.

64. H. Sugiura, T. Yamadaya, Raman scattering in silica glass in the permanent densification region, J. Non-Cryst. Solids 144 (1992) 151–158. https://doi.org/10.1016/S0022-3093(05)80395-3.

65. F.L. Galeener, Planar rings in vitreous silica, J. Non-Cryst. Solids 49(1–3) (1982) 53–62. https://doi.org/10.1016/0022-3093(82)90108-9.

66. M. Heili, B. Poumellec, E. Burov, C. Gonnet, C. Le Losq, D.R. Neuville, M. Lancry, The dependence of Raman defect bands in silica glasses on densification revisited, J. Mater. Sci. 51 (2016) 1659–1666. https://doi.org/10.1007/s10853-015-9489-8.

67. W.B. White, B.A. DeAngelis, Interpretation of the vibrational spectra of spinels, Spectrochim. Acta 23A (1967) 985–995. https://doi.org/10.1016/0584-8539(67)80023-0.

68. A. Chopelas, A. M. Hofmeister, Vibrational spectroscopy of aluminate spinels at 1 atm and of $MgAl_2O_4$ to over 200 kbar, Phys. Chem. Miner. 18 (1991) 279–293. https://doi.org/10.1007/BF00200186.

69. S. Lopez-Moreno, P. Rodriguez-Hernandez, A. Munoz, A.H. Romero, F.J. Manjon, D. Errandonea, E. Rusu, V.V. Ursaki, Lattice dynamics of $ZnAl_2O_4$ and $ZnGa_2O_4$ under high pressure, Ann. Phys. 523 (1–2) (2011) 157–167. https://doi.org/10.1002/andp.201000096.

70. M.C. Oliveira, R.A.P. Ribeiro, E. Longo, M.R.D. Bomio, S.R. de Lázaro, Quantum mechanical modeling of Zn-based spinel oxides: Assessing the structural, vibrational, and electronic properties, Int. J. Quantum. Chem. 120(22) (2020) e26368(1–13). https://doi.org/10.1002/qua.26368.

71. H. Cynn, S.K. Sharma, T.F. Cooney, M. Nicol, High-temperature Raman investigation of order-disorder behavior in the $MgAl_2O_4$ spinel, Phys. Rev. B 45 (1992) 500–502. https://doi.org/10.1103/physrevb.45.500.

72. V. Mohacek-Grosev, M. Vrankic, A. Maksimovic, V. Mandi, Influence of titanium doping on the Raman spectra of nanocrystalline $ZnAl_2O_4$, J. Alloys Compd. 697 (2017) 90–95. https://doi.org/10.1016/j.jallcom.2016.12.116.

73. I.P. Alekseeva, O.S. Dymshits, V.V. Golubkov, P.A. Loiko, M.Ya. Tsenter, K.V. Yumashev, S.S. Zapalova, A.A. Zhilin, Influence of NiO on phase transformations and optical properties of $ZnO–Al_2O_3–SiO_2$ glass-ceramics nucleated by TiO_2 and ZrO_2. Part I. Influence of NiO on phase transformations of $ZnO–Al_2O_3–SiO_2$ glass-ceramics nucleated by TiO_2 and ZrO_2, J. Non-Cryst. Solids 384 (2014) 73–82. https://doi.org/10.1016/j.jnoncrysol.2013.05.038.

74. T. Mazza, E. Barborini, P. Piseri, P. Milani, D. Cattaneo, A. Li Bassi, C. E. Bottani, C. Ducati, Raman spectroscopy characterization of TiO_2 rutile nanocrystals, Phys. Rev. B 75 (2007) 045416(1–5). https://doi.org/10.1103/PhysRevB.75.045416.

75. O. Frank, M. Zukalova, B. Laskova, J. Kürti, J. Koltai, L. Kava, Raman spectra of titanium dioxide (anatase, rutile) with identified oxygen isotopes (16, 17, 18), Phys. Chem. Chem. Phys. 14 (2012) 14567–14572. https://doi.org/10.1039/C2CP42763J.

76. V. D'Ippolito, G. B. Andreozzi, D. Bersani, P. P. Lottici, Raman fingerprint of chromate, aluminate and ferrite spinels, J. Raman Spectrosc. 46 (2015) 1255–1264. https://doi.org/10.1002/jrs.4764.

77. D. Levy, G. Artioli, Thermal expansion of chromites and zinc spinels, Mater. Sci. Forum, 278–281 (1998) 390–395. https://doi.org/10.4028/www.scientific.net/MSF.278-281.390.

78. D. Hummer, P. Heaney, J. Post, Thermal expansion of anatase and rutile between 300 and 575 K using synchrotron powder X-ray diffraction, Powder Diffr., 22(4) (2007) 352–357. https://doi.org/:10.1154/1.2790965.

79. P. Schultz, H. Smyth, Ultra-low expansion glasses and their structure in the SiO_2-TiO_2 system, Amorphous Materials, Wiley Interscience 1970, pp. 453–461.

80. K. Kamiya, S. Sakka, Thermal expansion of TiO_2-SiO_2 and TiO_2-GeO_2 glasses, J. Non-Cryst. Solids 52 (1982) 357–363. https://doi.org/10.1016/0022-3093(82)90310-6.

81. D.R. Peacor, High-temperature single-crystal study of the cristobalite inversion, Z. Kristallogr. 138 (1973) 274–298. https://doi.org/10.1524/zkri.1973.138.1-4.274.

82. A. Hunger, G. Carl, A. Gebhardt, C. Rüssel, Ultra-high thermal expansion glass–ceramics in the system $MgO/Al_2O_3/TiO_2/ZrO_2/SiO_2$ by volume crystallization of cristobalite, J. Non-Cryst. Solids 354 (2008) 5402–5407. https://doi.org/10.1016/j.jnoncrysol.2008.09.001.

83. L. Basyrova, V. Bukina, S. Balabanov, A. Belyaev, V. Drobotenko, O. Dymshits, I. Alekseeva, M. Tsenter, S. Zapalova, A. Khubetsov, A. Zhilin, A. Volokitina, V. Vitkin, X. Mateos, J.M. Serres, P. Camy, P. Loiko, Synthesis, structure and spectroscopy of Fe^{2+}:$MgAl_2O_4$ transparent

ceramics and glass-ceramics, J. Lumin. 236 (2021) 118090(1–17). https://doi.org/10.1016/j.jlumin.2021.118090.

84. H.K. Mao, P.M. Bell, D. Virgo, Crystal-field spectra of fassaite from the Angra dos Reis meteorite, Earth Planet. Sci. Lett. E, 35(2) (1977) 352–356. https://doi.org/10.1016/0012-821X(77)90137-6.

85. D.A. Nolet, R.G. Burns, S.L. Flamm, J.R. Besancon, Spectra of Fe-Ti silicate glasses: Implications to remote-sensing of planetary surfaces, Proceedings of Lunar and Planetary Science Conference, 10th, Houston, Tex., March 19-23, 1979. Volume 2. (A80–23617 08–91) New York, Pergamon Press, Inc., 1979, p. 1775–1786. https://api.semanticscholar.org/CorpusID:93151285.

86. A.S. Marfunin, Physics of minerals and inorganic materials: an introduction, Springer-Verlag, Berlin, Heidelberg, New York, 1979, 340 pp.

87. B.M. Loeffler, R.G. Burns, J.A. Tossell, D.J. Vaughan, K.H. Johnson, Charge transfer in lunar materials: interpretation of ultraviolet-visible spectral properties of the moon, Proceedings of the Fifth Lunar Conf., Supplement 5, Geochim. Cosmochim. Acta, 3(1974) 3007–3016.

88. G.H. Faye, D.C. Harris, On the origin and pleochroism in andalusite from Brazil, Can. Mineral. 10 (1969) 47–56.

89. R.G. Burns, Intervalence transitions in mixed valence minerals of iron and titanium, Ann. Rev. Earth Planet. Sci. 9 (1981) 345–383. https://doi.org/10.1146/annurev.ea.09.050181.002021.

90. K. Morinaga, H. Yoshida, H. Takebe, Compositional dependence of absorption spectra of Ti^{3+} in silicate, borate, and phosphate glasses, J. Am. Ceram. Soc. 77 (1994) 3113–3118. https://doi.org/10.1111/j.1151-2916.1994.tb04557.x.

91. N.A. El-Shafi, M.M. Morsi, Optical absorption and infrared studies of some silicate glasses containing titanium, J. Mater. Sci. 32 (1997) 5185–5189. https://doi.org/10.1023/A:1018685904770.

92. L.H.C. Andrade, S.M. Lima, A. Novatski, A.M. Neto, A.C. Bento, M.L. Baesso, F.C.G. Gandra, Y. Guyot, G. Boulon, Spectroscopic assignments of Ti^{3+} and Ti^{4+} in titanium-doped OH^- free low-silica calcium aluminosilicate glass and role of structural defects on the observed long lifetime and high fluorescence of Ti^{3+} ions, Phys. Rev. B 78 (2008) 224202(1–11). https://doi.org/10.1103/PhysRevB.78.224202.

93. A. Grzechnik, P.F. McMillan, Temperature dependence of the OH^- absorption in SiO_2 glass and melt to 1975 K, Am. Min., 83 (1998) 331–338. https://doi.org/10.2138/am-1998-3-417.

94. R. Balzer, H. Behrens, T. Waurischk, S. Reinsch, R. Müller, P. Kiefer, J. Deubener, M. Fechtelkord, Water in alkali aluminosilicate glasses, Front. Mater. 7 (2020) Article 85 1–17. https://doi.org/10.3389/fmats.2020.00085.

95. A. Jouini, H. Sato, A. Yoshikawa, T. Fukuda, G. Boulon, G. Panczer, K. Kato, E. Hanamura, Ti-doped $MgAl_2O_4$ spinel single crystals grown by the micro-pulling-down method for laser application: Growth and strong visible blue emission. J. Mater. Res. 21, (2006) 2337–2344. https://doi.org/10.1557/jmr.2006.0280.

96. A. Jouini, A. Yoshikawa, A. Brenier, T. Fukuda, G. Boulon, Optical properties of transition metal ion-doped $MgAl_2O_4$ spinel for laser application, Phys. Stat. Sol. (c) 4(3) (2007) 1380–1383. https://doi.org/10.1002/pssc.200673872.

97. P.F. Moulton, J.G. Cederberg, K.T. Stevens, G. Foundos, M. Koselja, J. Preclikova, Characterization of absorption bands in Ti:sapphire crystals, Opt. Mater. Express 9(5) (2019) 2216–2251. https://doi.org/10.1364/OME.9.002216.

98. M. Vrankić, B. Gržeta, V. Mandić, E. Tkalčec, S. Miloševic, M. Čeh, B. Rakvin, Structure, microstructure and photoluminescence of nanocrystalline Ti-doped gahnite, J. Alloys Compd. 543 (2012) 213–220. http://dx.doi.org/10.1016/j.jallcom.2012.07.073.

99. A. Sanchez, A.J. Strauss, R.L. Aggarwal, R.E. Fahey, Crystal growth, spectroscopy, and laser characteristics of Ti:$A1_2O_3$, IEEE J. Quantum Electron. 24(6) (1988) 995–1002. https://doi.org/10.1109/3.220.

100. V.M. Khomenko, K. Langer, H. Rager, A. Fett, Electronic absorption by Ti^{3+} ions and electron delocalization in synthetic blue rutile. Phys. Chem. Miner. 25 (1998) 338–346. https://doi.org/10.1007/s002690050124.

101. V.T. Gritsyna, Yu.G. Kazarinov, V.A. Kobyakov, L.A. Lytvynov, Growth and characterization of titanium doped spinel crystals, Acta Phys. Pol. A. 133(4) (2018) 774–777. https://doi.org/10.12693/APhysPolA.133.774.

102. J.W. Anthony, R.A. Bideaux, K.W. Bladh, M.C. Nichols, "Gahnite" (PDF). Handbook of Mineralogy. Mineral Data Publishing. (2005). Retrieved 14 March 2022.

103. O. Medenbach, T. Siritanon, M.A. Subramanian, R.D. Shannon, R.X. Fischer, G.R. Rossman, Refractive index and optical dispersion of In_2O_3, $InBO_3$ and gahnite, Mater. Res. Bull. 48(6) (2013) 2240–2243. https://doi.org/10.1016/j.materresbull.2013.02.057.

104. W.L. Bond, Measurement of the refractive indices of several crystals, J. Appl. Phys. 36 (1965) 1674–1677. https://doi.org/10.1063/1.1703106.

105. M.P. Shepilov, O.S. Dymshits, A.A. Zhilin, V.V. Golubkov, A.E. Kalmykov, I.P. Alekseeva, A.V. Myasoedov, A.A. Hubetsov, S.S. Zapalova, Effect of low NiO doping on anomalous light scattering in zinc aluminosilicate glass-ceramics, J. Non-Cryst. Solids 473 (2017) 152–169. https://doi.org/10.1016/j.jnoncrysol.2017.08.012.

106. M. Shepilov, O. Dymshits, A. Zhilin, A simple method for estimation of the scattering exponent of nanostructured glasses, Mater. 16 (2023) 2630(1–24). https://doi.org/10.3390/ma16072630.

107. A.S. Perera, J.K. Cockcroft, P. Trogadas, H. Yu, N. Kapil, M.-O. Coppens, Titanium(IV)-induced cristobalite formation in titanosilicates and its potential impact on catalysis, J. Mater. Sci. 54 (2019) 335–345. https://doi.org/10.1007/s10853-018-2869-0.

108. G.D. Bromiley, J. Brooke, S.C. Kohn, Hydrogen and deuterium diffusion in non-stoichiometric spinel, High Press. Res. 37(3) (2017) 360-376. https://doi.org/10.1080/08957959.2017.1353091.

109. E. Libowitzky, G.R. Rossman, An IR absorption calibration for water in minerals, Am. Mineral. 82 (1997) 1111–1115. https://doi.org/10.2138/am-1997-11-1208.

110. E. Libowitzky, Correlation of O-H stretching frequencies and O-H…O hydrogen bond lengths in minerals, Monatsh. Chem. 130 (1999) 1047–1059. https://doi.org/10.1007/BF03354882.

111. C. Closmann, Q. Williams, In-situ spectroscopic investigation of high-pressure hydrated (Mg,Fe)SiO_3 glasses: OH vibrations as a probe of glass structure, Am. Mineral. 80 (1995) 201–212. http://www.minsocam.org/MSA/AmMin/TOC/Articles_Free/1995/Closmann_p201-212_95.pdf.

112. A. Beran, E. Libowitzky, Water in natural mantle minerals II: olivine, garnet and accessory minerals, Rev. Mineral. Geochem. 62 (1) (2006) 169–191. https://doi.org/10.2138/rmg.2006.62.8.

113. D. Lenaz, H. Skogby, F. Nestola, F. Princivalle, OH incorporation in nearly pure $MgAl_2O_4$ natural and synthetic spinels, Geochimica et Cosmochimica Acta, 72(2) (2008) 475–479, https://doi.org/10.1016/j.gca.2007.10.020.

114. D.-L. Ge, Y.-J. Fan, C.-L. Qi, Z.-X. Sun, Facile synthesis of highly thermostable mesoporous $ZnAl_2O_4$ with adjustable pore size, J. Mater. Chem. A 1 (2013) 1651–1658. https://doi.org/10.1039/C2TA00903J.

115. M.M. Halmer, E. Libowitzky, A. Beran, IR spectroscopic determination of OH defects in spinel group minerals, Publication: EGS - AGU - EUG Joint Assembly, Abstracts from the meeting held in Nice, France, 6 – 11 April 2003, abstract id. 6742. 2003EAEJA.....6742H.

116. D. Kohlstedt, H. Keppler, D. Rubie, Solubility of water in the *α, β and γ* phases of $(Mg,Fe)_2SiO_4$. Contrib. Mineral. Petrol. 123 (1996) 345–357. https://doi.org/10.1007/s004100050161

117. G.E. Walrafen, S.R. Samanta, Infrared absorbance spectra and interactions involving OH groups in fused silica, J. Chem. Phys. 69 (1978) 493–495. https://doi.org/10.1063/1.436379.